

1 **The stratigraphic record and processes of turbidity current transformation across deep-**
2 **marine lobes**

3

4 Ian Kane^{1*}, Anna Pontén², Brita Vangdal³, Joris Eggenhuisen⁴, David M. Hodgson⁵, Yvonne T.
5 Spsychala^{5,4}

6 ¹*Statoil ASA, Exploration, NO-1364, Oslo, Norway*

7 ²*Statoil ASA, Research Centre Rotvoll, NO-7005 Trondheim, Norway*

8 ³*Statoil ASA, Research Centre Bergen, NO-5020, Bergen, Norway*

9 ⁴*Faculty of Geosciences, Utrecht University, PO Box 80021, 3508TA Utrecht, The Netherlands*

10 ⁵*School of Earth and Environment, University of Leeds, LS2 9JT, United Kingdom*

11 **Present address: School of Earth, Atmospheric and Environmental Sciences, University of*
12 *Manchester, Oxford Road, Manchester M13 9PL, United Kingdom*

13 **Abstract**

14 Sedimentary facies in the distal parts of deep-marine lobes can diverge significantly from those
15 predicted by classical turbidite models, and sedimentological processes in these environments are
16 poorly understood. This gap may be bridged using outcrop studies and theoretical models. In the
17 Skoorsteenbergt Fm., a downstream transition from thickly-bedded turbidite sandstones to
18 argillaceous, internally layered hybrid beds is observed. The hybrid beds have a characteristic
19 stratigraphic and spatial distribution, being associated with bed successions which generally coarsen-
20 and thicken-upwards reflecting deposition on the fringes of lobes in a dominantly progradational
21 system. Using a detailed characterisation of bed types, including grain size, grain fabric and
22 mineralogical analyses, a process-model for flow evolution is developed. This is explored using a
23 numerical suspension capacity model for radially spreading and decelerating turbidity currents. The
24 new model shows how decelerating sediment suspensions can reach a critical suspension capacity
25 threshold beyond which grains are not supported by fluid turbulence. Sand and silt particles, settling
26 together with flocculated clay, may form low yield-strength cohesive flows; development of these
27 higher concentration lower boundary layer flows inhibits transfer of turbulent kinetic energy into the
28 upper parts of the flow ultimately resulting in catastrophic loss of turbulence and collapse of the
29 upper part of the flow. Advection distances of the now transitional to laminar flow are relatively
30 long (several km) suggesting relatively slow dewatering (several hours) of the low yield strength

31 flows. The catastrophic loss of turbulence accounts for the presence of such beds in other fine-
32 grained systems without invoking external controls or large-scale flow partitioning, and also
33 explains the abrupt pinch-out of all divisions of these sandstones. Estimation of the point of flow
34 transformation is a useful tool in the prediction of heterogeneity distribution in subsurface systems.

35 *Keywords: Hybrid beds, transitional flow deposits, flow transformation, deep-marine channels and*
36 *lobes, reservoir quality, flow capacity, Karoo*

37

38 **Introduction**

39 Observation and interpretation of sedimentary facies from deep-marine lobe deposits has been
40 strongly influenced by models developed from relatively small and coarse-grained basins, for
41 example the Annot sub-basins (Bouma, 1962) and the Californian Borderlands (Lowe, 1982).
42 However, today's ultra-deep-water subsurface exploration targets are typically associated with
43 sedimentary systems that are up to orders of magnitude larger, drained much larger areas, and are
44 significantly finer grained (e.g. the Wilcox Fm. of the Gulf of Mexico, Zarra et al., 2007). The
45 sedimentary environments and facies distributions of these systems are understudied as they
46 commonly develop on passive margins and may overlie transitional or oceanic crust, and as such are
47 prone to subduction. Numerous studies have documented these systems from remote sensing-based
48 observations and slightly more limited core data from the modern and Holocene stratigraphy (an
49 excellent example being the Mississippi Fan, see summary in Twichell et al., 2009). Due to the
50 paucity of outcrops revealing such systems, it may be appropriate to use fine-grained systems in
51 smaller basins as process analogues to larger systems (e.g. Martinsen et al., 2000; Sullivan et al.,
52 2000). In these fine-grained systems, complicated facies and facies distributions, which diverge
53 significantly from classical turbidite models, are reported from medial and distal lobe settings
54 (Haughton et al., 2003, 2009; Sylvester & Lowe, 2004; Talling et al., 2004, 2012; Amy & Talling,
55 2006; Ito, 2008; Barker et al., 2008; Davies et al., 2009; Hodgson, 2009; Kane & Pontén, 2012;
56 Pyles & Jennette, 2012; Talling, 2013; Grundvåg et al., 2014; Terlaky & Arnott, 2014; Fonnesu et
57 al., 2015; Southern et al., 2015, 2016; Sychala et al., in press). Such beds have been termed hybrid
58 event beds by Haughton et al. (2009), which emphasises that an individual bed represents the
59 deposits of different types of flow within the same event. Typically, this is a basal turbidite and an
60 upper debrite; the term has, however, been adopted to cover a wide range of deposit and process
61 types which combine to form a single 'hybrid' bed (e.g., Hodgson, 2009; Talling, 2013; Fonnesu et

62 al., 2015). The stratigraphic and spatial complexity of these bed types means that deep-marine fan
63 systems represent significant challenges for reservoir prediction at both exploration and development
64 scales (Porten et al., in press). The Paleogene Wilcox Fm. exemplifies these challenges: it is
65 characterised by extremely large volumes of sandstone, but often occurring as mud-rich sandstones
66 with marginal reservoir quality (i.e., low porosity and permeability values), with stratigraphically
67 and spatially isolated higher-quality reservoir sandstones (Zarra, 2007; Kane and Pontén, 2012).

68 In this contribution, the spatial and stratigraphic distribution of the various sedimentary facies
69 associated with proximal, medial and distal deep-marine lobe environments of Fan 3,
70 Skoorsteenberg Fm., Tanqua Karoo, are presented and characterised, with particular emphasis on
71 hybrid beds. The paper comprises two interlinked sections, with the main focus being 1) to
72 characterise fine-grained hybrid beds, and 2) to develop a process based numerical model for their
73 observed occurrence. In the first part, we use outcrop and petrological observations to infer
74 sedimentological flow processes. In the second part, a numerical model is introduced to investigate
75 the inferred processes. The model uses a suspension-capacity model (Eggenhuisen et al., 2016), and
76 applies it to radially spreading decelerating flows. Integrating the detailed bed characterisation and
77 the numerical model, we propose that these types of hybrid beds form due to the loss of turbulence
78 due to flow deceleration, the development of internal stratification and eventual catastrophic loss of
79 turbulence in the flow. Understanding of the process sedimentology of these deposits and their
80 stratigraphic and spatial distribution can be applied to systems of similar grain-size range to
81 significantly reduce subsurface uncertainty and to improve prediction.

82

83 **Data and Methods**

84 The dataset comprises 20 sedimentological logs collected in the field and correlated by walking out
85 individual beds (Fig. 1). These logs were collected at 1:20 scale with more detailed logs of
86 individual beds and packages of beds collected at 1:2 scale (Figs. 2-5). Aerial photographs supported
87 field correlation in areas that were difficult to access or were covered (Fig. 2). Data collected
88 include lithology, bed thickness, and palaeocurrent measurements from ripples, flutes and other sole
89 marks. In addition, the equivalent stratigraphic intervals within cores from 7 research boreholes were
90 logged at 1:20 scale (Fig. 3).

91 Petrographic analysis was performed from 49 orientated thin sections. Although not strongly
92 cemented, point-counting is challenging due to the high degree of compaction and commonly large
93 proportion of clay. For this reason, further analytical work using the QEMSCAN[®] (Quantitative
94 Evaluation of Minerals by SCANNing electron microscopy) was undertaken on 39 samples to
95 quantitatively analyse the mineralogy and texture of different bed types in order to support
96 qualitative outcrop observations. QEMSCAN[®] uses an FEI Quanta 650F SEM (Scanning Electron
97 Microscope) with two silicon drift energy-dispersive X-ray spectrometers (Pirrie et al., 2004). X-ray
98 and backscattered electron signals are used to image and create quantified mineralogical maps of
99 thin sections with a resolution of 5 µm). Typically, framework mineral grains are isolated within, or
100 coated by, the clay matrix and they can be imaged separately by the QEMSCAN[®]. These grains can
101 be measured and grain size distributions made from the resultant large datasets (1×10^5 - 2×10^6 grains
102 per section). Grain size is determined according to the long axis, which is automatically measured in
103 thin section. As with traditional thin-section point-counting, this method underestimates grain-size
104 diameter by 11%, or by 0.2 phi units (Johnson, 1994). The smallest grains measured are 5 µm, which
105 does not significantly truncate the fine tail end of the grain size spectrum.

106

107 **Geological setting of the Karoo Basin, Tanqua Depocentre and Skoorsteenberg Fm.**

108

109 During the Permian, the Karoo Basin is interpreted as either a retro-arc foreland basin developed
110 inboard of a fold and thrust belt (De Wit and Ransome, 1992; Veevers et al., 1994; Visser and
111 Prackelt, 1996; Visser, 1997; López-Gamundí and Rossello, 1998), or, to subsidence caused by
112 dynamic topography related to subduction (Pysklywec and Mitrovica, 1999; Tankard et al., 2009).
113 The Tanqua depocentre (Fig. 1A) was a topographic 'low' developed within the south-western part
114 of the Karoo Basin, and is bound by an oroclinal bend in the Cape Fold Belt, with the Cederberg
115 branch bounding the western margin and the Swartberg Branch bounding the southern margin. The
116 depocentre is filled by sediments of Westphalian (Carboniferous) to Triassic age, which comprise
117 the Karoo Supergroup. These sediments record the late Palaeozoic deepening and then shallowing of
118 the basin (Hodgson, 2009). The Karoo Supergroup is subdivided into the glaciogenic Dwyka Group
119 (Westphalian to early Permian), the marine Ecca Group (Permian) (Fig. 1C) and the non-marine
120 Beaufort Group (Permo-Triassic) (Smith, 1990).

121 In the Tanqua depocentre, the Ecca Group comprises an approximately 1400 m thick
122 succession of siliciclastic sediments (Wickens, 1994; King et al., 2009). The lower Ecca Group (the

123 Prince Albert, Whitehill, and Collingham formations) is overlain by >600 m of mudstone and
124 siltstone (Tierberg Fm.; Hodgson et al., 2006), which in turn is overlain by a c.400 m thick fine-
125 grained interval of sand-rich submarine fans, separated by extensive claystone and siltstone intervals,
126 forming the progradational Skoorsteenberg Fm. (Wickens, 1994; Morris et al., 2000; Johnson et al.,
127 2001; Wild et al., 2005; Hodgson et al., 2006, Hodgson 2009; Prélat et al., 2009; Spychala et al., in
128 revision) (Fig. 1). The Kookfontein Fm. overlies the Skoorsteenberg Fm. and is a c.300 m thick
129 succession representing a submarine slope and shelf-edge delta, shallowing-up to deltaic and
130 shoreface deposits (Wild et al., 2009; Poyatos-More et al., 2016).

131

132 ***Skoorsteenberg Fm.***

133 The c. 400 m thick Skoorsteenberg Fm. consists of five fine-grained sandy intervals, interpreted as
134 four submarine fans (Fans 1-4) and an overlying base-of-slope to lower slope succession termed Unit
135 5 (Bouma & Wickens, 1991; Wickens, 1994; Morris et al., 2000; Johnson et al., 2001; Wild et al.,
136 2005; Hodgson et al., 2006) (Fig. 1). To retain consistency with previous literature, the ‘fan’
137 nomenclature is retained, which has been used as a lithostratigraphic term and encompasses a linked
138 system of sandstone and siltstone channel-fills and lobe bodies. Collectively, the lobes of Fan 3 may
139 be regarded as a lobe-complex set (c.f. Prélat et al., 2009). A robust stratigraphic framework for the
140 formation has been established by several field studies (Wickens and Bouma, 1991; Wickens, 1994;
141 Bouma and Wickens, 2001; Johnson et al., 2001; Hodgson et al., 2006; Hodgson, 2009; Prélat et al.,
142 2009; Hofstra et al., 2015). This has been augmented by seven research boreholes and together this
143 has allowed the development of a detailed evolutionary model for the fan intervals (Hodgson et al.,
144 2006; Luthi et al., 2006). Fan 3 is interpreted to record a pattern of initiation, followed by
145 progradation and aggradation, to retrogradation (Hodgson et al., 2006). Within a sequence
146 stratigraphic framework, each fan has been interpreted to represent a lowstand systems tract and the
147 overlying regional claystone and siltstone as the combined transgressive and highstand systems tract
148 (Goldhammer et al., 2000; Johnson et al., 2001; Hodgson et al., 2006). The chronostratigraphic
149 framework for the fans remains poorly constrained, although recently published U–Pb single-grain
150 zircon ages from volcanic ash layers indicate an overall late Permian age (c.255 Ma, Fildani et al.,
151 2007, 2009; McKay et al., 2015).

152 Lithofacies of the submarine fans have been described previously (Morris et al., 2000;
153 Sullivan et al., 2000; Johnson et al., 2001; van der Werff and Johnson, 2003a, 2003b; Hodgson et al.,
154 2006; Hodgson, 2009; Prélat et al., 2009; Groenenberg et al., 2010; Jobe et al., 2012; Hofstra et al.,
155 2015). This study focuses on hybrid beds within Fan 3, which have been described previously as bi-

156 and tri-partite turbidites with slurry or debris flow caps (Morris et al., 2000; Johnson et al., 2001;
157 Hodgson et al., 2006; Luthi et al., 2006). Hodgson (2009) expanded on this work and interpreted
158 these beds as ‘hybrid beds’ (equivalent to ‘hybrid event beds’ *sensu* Haughton et al., 2009). Hodgson
159 (2009) interpreted the upper parts of these composite beds as 1) the deposits of debris-flows derived
160 from partial flow transformation after shelf-edge collapse; 2) developed through flow transformation
161 from turbidity currents entraining a muddy substrate; or 3) representing the mudstone clast-rich tails
162 of turbidity currents where the matrix was not argillaceous. Johnson et al. (2001) and Hodgson et al.
163 (2009) noted a preferential geographic distribution of these beds at the fringes of lobe deposits, with
164 Hodgson (2009) attributing a preferential stratigraphic distribution at the base of lobe complexes to
165 slope incision during fan initiation and progradation phases.

166

167 **Results**

168 **Lithofacies**

169 The lithofacies presented here represent ‘event beds’ and are classified based on outcrop
170 observations (Figs. 2-7) following the approach of Johnson et al. (2001), Hodgson et al. (2006) and
171 Hodgson (2009), utilising the latter’s four-fold lithofacies scheme, which is particularly relevant to
172 the fringe facies of lobes. The detailed characterisation of samples from individual beds, presented
173 below is used to support the necessary degree of interpretation of features from outcrop, e.g., mud
174 content (n.b. ‘mud’ is used here as a general term for mixtures of clay, silt, organic fragments and
175 clay flocs and clasts). Nevertheless, outcrop-based observations/interpretations of relative clay-
176 content closely match quantitative data from analytical techniques, giving confidence in this
177 approach. Therefore, the analysis below is based on outcrop and core observations and provides a
178 framework for the more detailed analyses that follow.

179 *Thick-bedded sandstones (0.6-6 m)*

180 Thick-bedded sandstones are very-fine to fine-grained, generally lacking primary structures but may
181 be marked by dewatering structures, predominantly pillars and lesser dishes; these are subtle features
182 at outcrop and are more clearly visible in core (Fig. 8H). These ‘beds’ are often amalgams of several
183 beds (e.g., capping Lobe 5, Fig. 2A and C; and Log SK3, Fig. 4). Bed amalgamation can be
184 enigmatic in outcrop, but is more readily observed in core, where typical features comprise
185 mudstone rip-up clasts, subtle grain size changes and truncated dewatering structures. Rarely, bed

186 tops preserve some tractional structures, plane parallel-lamination and ripple cross-lamination, in
187 conjunction with a normal grading profile. Bed bases are sharp, and commonly truncate underlying
188 beds in angular steps (Fig. 6B). Flutes and tool marks are present, but not common. It is less
189 common to see loading at the bases of these thick beds than the thinner-bedded sandstones.

190 Interpretation: Characteristic features of turbulent flow, such as flutes, tools, normal grading and
191 tractional structures suggest that these beds are turbidites. The general lack of structure throughout
192 most of these beds might in part reflect the often pervasive dewatering, which is apparent in core,
193 but generally not at outcrop. Hodgson (2009) suggests that the overall fine grain size, and its narrow
194 range, preclude the interpretation of flow concentration and sub-division into low-, medium- or high-
195 density turbidites, although tractional structures are generally well developed in many of the thinner
196 turbidites. Based on the observations above and the further discussion of mineralogical and textural
197 data presented below, these deposits are interpreted for the most part as high-density turbidites,
198 *sensu* Lowe (1982).

199 *Thin-to-medium bedded sandstones (0.1-0.6 m)*

200 Very-fine to fine-grained sandstones are generally normally-graded and dominated by tractional
201 structures (ripple- and plane-parallel lamination) (e.g., see Log SK5, interval 7-9 m); in outcrop
202 tractional structures can be very subtle (Fig. 8A). The lower parts of beds may be structureless. Bed
203 bases are sharp, flat lying, and may be marked by flute casts, whilst bed tops may contain abundant
204 organic material and mudstone clasts in a clean sand matrix, and may preserve ripple forms. Banding
205 occurs in some parts of the fan, but can be difficult to discern in the field, being clearer in core (Fig.
206 8F).

207 Interpretation: Based on their tractional structuration, normal grading and flute casts, beds of this
208 lithofacies are interpreted as low- to medium-density turbidites deposited by low- to medium-
209 concentration turbidity currents (*sensu* Lowe, 1982). Banding may reflect some periodic suppression
210 of turbulence associated with flow deceleration or increased concentration (Lowe & Guy, 2000;
211 Barker et al., 2008).

212 *Siltstones and thin-bedded sandstones (individual beds <0.1 m)*

213 This lithofacies comprises siltstone to very-fine grained sandstone beds that are commonly
214 interbedded (e.g., interval 1.5-2.5 m, Log Sk20, Fig. 4; Fig. 7). These are typically normally-graded,
215 plane-parallel laminated and/or ripple cross-laminated and sometimes have small flute and tool

216 marks on their bases. In the distal parts of lobes (Prelat et al., 2009) climbing ripple lamination,
217 common in proximal areas, is not observed.

218 Interpretation: Their tractional structuration and normal grading leads to an interpretation of these
219 beds as turbidites deposited by low-density turbidity currents (*sensu* Lowe, 1982).

220 *Hybrid beds*

221 The focus of this study is the character and prevalence of hybrid beds in frontal lobe fringe deposits
222 (*sensu* Spychala et al. in revision). Frontal fringe here denotes the distal and frontal part of the lobes,
223 approximately 5 km from their pinch-out, following and consistent with Hodgson (2009) and Pr elat
224 and Hodgson (2013), and approximately 25-30 km downdip from the channelized to unconfined
225 areas. In contrast, lateral lobe fringes have rare hybrid beds and are dominated by low-density
226 traction-dominated turbidites (Spychala et al. 2016; in revision). There is a wide range of lithofacies
227 within the hybrid-bed class, and these can be laterally variable within individual beds over the scale
228 of tens of centimetres (Fig. 7). There is a general down-flow progression from deposits that appear
229 more turbiditic to deposits with the character of debrites.

230

231 *Thick-bedded hybrid beds (0.6-1.2 m)*

232 These occur approximately 5 km from pinch-out. Commonly, thick (up to 1.2 m) beds with stepwise
233 basal erosional cuts (cm-decimetre scale) into the substrate that lack loading and other soft-sediment
234 deformational structures (e.g., bed at 5.4 m SK5, Fig. 4). Beds are generally graded throughout with
235 upper parts that are slightly more clay rich (c. 5-10%, see mineralogy section) and commonly clast
236 rich. These are similar to the thick-bedded turbidites described above but form part of a continuum
237 with the deposits described below, characterised by increasing mud content at bed tops.

238 *Interpretation*

239 In the channel-fills and scour-fills at and beyond the channel-lobe transition (e.g., Hofstra et al.,
240 2015), erosion and entrainment of the weakly consolidated substrate resulted in sharp basal surfaces
241 to turbidites, and the incorporation of intrabasinal clasts. This erosional behaviour seems to have
242 persisted across much of the proximal and medial part of the lobes, at least associated with the larger
243 events, to these relatively distal positions. Entrained substrate was rapidly broken up within the flow
244 often resulting in clast and clay-rich divisions at bed tops. The absence of soft-sediment deformation
245 structures in the underlying substrate is interpreted to be due to excavation of the soft substrate to a

246 firm layer where the substrate shear strength is greater than that of the shear stress exerted by the
247 overriding flow.

248
249 *Thin- to medium-bedded hybrid beds (0.1-0.6 m)*
250 These occur approximately 3 km from pinch-out. Beds in this 'position' are complicated, with
251 intensely loaded bases and flame structures. Beds are a few to 60 cm thick, but pinch and swell as
252 they load into underlying substrate (e.g., bed at 1-2.5 m Log SK1, Fig. 4; 0-1 m Log SK4, Fig. 5;
253 Figs. 7A, 8). Locally, sections of substrate are fully or partially lifted into the bed. A patchy
254 development of internal layering is observed, with cleaner lower sandstone divisions (c. 10-15%
255 clay, see mineralogy section below), and muddier upper sandstone divisions (c. 30-35% clay) that
256 appear intermittently laterally and extend for 10's to 100's of cm. Rare thin silty caps are observed.

257
258 *Interpretation*

259 The description demonstrates interaction of an overriding flow with the substrate that, owing to the
260 lower energy of the flows compared to proximal areas, leaves a record of partial or incomplete
261 substrate entrainment. The development of internal layering and the lateral variability suggests that
262 flows increased in concentration but had not developed stable density stratification. The general lack
263 of a silty cap to these beds suggests that the material was mixed within the argillaceous upper parts
264 of these beds and that the flows were undergoing transformation.

265
266 *Thin-bedded hybrid beds (<0.1 m)*

267 These occur predominantly <1 km from pinch-out. Typically, bi- or tri-partite beds, although some
268 beds have four internal divisions (Figs. 7 & 8). From the base these divisions are: 1) a very-fine-
269 grained sandstone, which is relatively mud-poor with respect to the upper divisions, and always
270 lacking macroscopic tractional structuration. The boundary with the overlying division is typically
271 sharp and may be marked by bed-parallel mudstone clasts; 2) an argillaceous sandstone with a bed-
272 parallel or inclined shear fabric (Fig. 7); 3) a highly argillaceous sandstone with high organic
273 fragment content and a strongly sheared fabric; 4) rare examples have a siltstone cap. Additional
274 internal divisions of variable mud content are common and these typically have the characteristic
275 sheared appearance noted above. In outcrop, mud content is qualitatively determined by colour and
276 weathering style, with muddier beds typically having a more 'bulbous' nature or spherical

277 weathering pattern typical of homogenous rocks. Bed bases are flat to slightly undulose in distal
278 localities, sometimes slightly loaded with rare, small (mm-scale) flame structures.

279

280 *Interpretation*

281 The high mud content of these deposits suggests deposition from higher concentration flows than
282 their up-dip equivalents, which were depositing en-masse and potentially behaving as transitional to
283 laminar flows. The strong internal layering of these deposits is interpreted to reflect the development
284 of discrete rheological zones within the flow in response to radial spreading of flows, deceleration,
285 and increase in near bed flow concentration. The lowermost sand layer shows no evidence for
286 deposition by turbulent flow, being devoid of erosional or tractional structures with the exception of
287 rare grooves or tool marks, and has a high matrix content (see mineralogy section). Instead, the
288 sandier part of the bed is interpreted to represent the deposit of a high-concentration flow where
289 yield strength was the principal particle support mechanism. The basal layer is typically relatively
290 cleaner than the overlying layer(s) which may reflect the ability of the coarser particles in the flow to
291 settle to its base, suggesting the flow had relatively low strength (e.g., Sumner et al., 2009; Talling,
292 2013). Clasts along the intra-bed boundaries may represent kinetic sieving, with the larger clasts
293 working their way to the top of the lowermost bed division due to grain collisions in the low strength
294 transitional to laminar flows; alternatively, as grain collisions become less important (i.e., at higher
295 concentrations) buoyancy may have become more important. Upper bed divisions are interpreted to
296 be debris-flow deposits, based on their poor sorting and high matrix content (see *Mineralogy* section
297 below), suggesting a complete flow transformation took place. These divisions are interpreted to
298 reflect, in part, a longitudinal flow structure, rather than representing the one-to-one vertical
299 structure of the flow.

300

301 *Mineralogy*

302 Results:

303 Chemical and petrological analysis of thin sections has allowed the mineral composition of the
304 different facies types to be determined (Figs. 9-12). On a quartz-feldspar-lithic ternary diagram the
305 samples plot as lithic arkoses and feldspathic litharenites. An outcrop subdivision of samples into
306 ‘turbidites’ and ‘hybrid beds’ shows that turbidites fall entirely within the lithic arkose class, whilst
307 hybrid beds span the lithic arkose and feldspathic litharenite classes (Fig. 9). The wide range of
308 mineral types identified (Table 1 and Figs. 10 & 11) have been grouped together, for the purpose of

309 examining bed-scale mineralogical variability, into the following three classes, which together form
310 >90% of each sample: 1) quartz, 2) feldspar, and 3) clay. Of the clays, illite is most abundant; from
311 petrological analysis this appears to be primarily detrital in origin, although it could have been
312 altered from another detrital clay form, most-likely smectite or kaolinite; in either case it does not
313 appear to be a diagenetic mineral. In addition to detrital illite (or clay in general), there could be a
314 much smaller contribution from alteration of muscovite or feldspar (Fig. 12). The analysis reveals
315 distinctive mineralogical trends for the hybrid beds and turbidites (Fig. 13). Quartz is the dominant
316 detrital mineral, with slightly lower proportions of feldspar. Muscovite mica represents only 1-2% of
317 the mineral volume with no significant variability between hybrid beds or turbidites (Table 1).
318 Overall quartz is more abundant by proportion in the turbidites than in the hybrid beds, whereas
319 feldspar content remains approximately the same in both bed types (e.g., samples F and G; Fig. 13).
320 Clay content increases from bed bases to bed tops, with values in the lower parts of hybrid beds in
321 the range of 20-25%, compared to around 10% at the base of turbidites; this rises to 25-35% and 20-
322 25% respectively (Fig. 13).

323 **Interpretation:**

324 Compositional differences between hybrid beds and turbidites show a higher lithic content in the
325 former, which partly reflects the higher proportion of mudstone and siltstone clasts incorporated
326 within the hybrid beds. There is no significant difference in the heavy mineral distribution,
327 suggesting that flows across the lobes had a common source. The confirmation of higher mud
328 content in argillaceous divisions of hybrid beds validates the qualitative interpretations of mud
329 content based solely on outcrop observations presented both above and in Hodgson (2009). The
330 apparent strong internal layering of the hybrid beds observed at outcrop is clearly demonstrated to be
331 directly linked to mud content that gives good confidence in the interpretation of graphic logs
332 collected during this study. The relatively low clay content of turbidite sands is expected and has
333 been documented in other studies, e.g., Sylvester & Lowe (2004), and is accounted for by the fine
334 sediment being maintained in suspension as the coarser grains settle out.

335 ***Grain size***

336 ***Results:***

337 Grain size was determined using QEMSCAN[®]. Individual framework grain outlines (quartz and
338 feldspar) were extracted from the matrix material, to provide an overview of the 5-500 µm grain-size

339 spectrum. Grain size is illustrated as simple plots of trends within individual beds (Fig. 13), and as
340 entire grain-size distributions (Fig. 14). Peaks in the range of 200-500 μm are generally either
341 amorphous clay bodies or claystone clasts, and some minor cemented quartz grains. The grain-size
342 distribution curves illustrate the 'skew' of the grain size population, which can be described as
343 positively skewed when the sample has excess fine grained material (fine skewed), symmetrical,
344 when the distribution is even, or negatively skewed when the sample has an excess of coarse
345 material (e.g., Muiola and Weiser, 1968). In broad terms, turbidites have lower and middle divisions
346 characterised by positively skewed distributions, to symmetrical distributions in their upper
347 divisions, whereas hybrid beds are characterised by negatively skewed lower and middle divisions,
348 shifting to more symmetrical distributions in their upper parts (Fig. 15).

349 *Interpretation:*

350 The mean and maximum grain size of quartz and feldspar in turbidites is generally larger than in the
351 hybrid beds, suggesting that flow transformation took place sometime after the larger grains had
352 settled from suspension in turbulent flows. Typically, en-masse sedimentation would give a broad
353 positively skewed distribution, whilst a winnowed deposit, such as a beach sand, would be coarsely
354 skewed (Muiola and Weiser, 1968). The turbidites show a fine skew, indicating sedimentation of the
355 entire grain-size spectrum with minimal reworking, whereas the hybrid beds are coarsely skewed,
356 indicating that they have an excess of coarse grains in them. An explanation for this is that the
357 coarser grains were able to settle through a low yield strength muddy flow, akin to the late stage
358 settling described experimentally by Sumner et al. (2009). The upper parts of these beds, interpreted
359 as the deposits of higher yield strength flows to fully laminar flows, are characterised by
360 symmetrical distributions reflecting the full grain size distribution available during flow and
361 deposition.

362

363 *Fabric analysis*

364 Grain orientation is constrained using the least-projection method, which is defined as the direction
365 of the two most-closely spaced parallel lines that can be drawn tangentially to the edges of the
366 longest section of a grain (Dapples and Rominger 1945; Baas et al. 2007). Grain-fabric analysis
367 allows inferences of flow conditions to be made where macroscopic structures are not present.
368 Alignment of long axes occurs in most depositional regimes (although not all, see review by Baas et

369 al. 2007). The samples are devoid of macroscopic tractional structuration meaning that problems
370 regarding the orientation of long-axes with regards to palaeoflow, such as the presence of flow-
371 oblique fabrics or flow-transverse fabrics (typical of ripple cross-lamination), are avoided (see
372 Hiscott & Middleton 1980; Baas et al. 2007, and references therein). The purpose of the analysis is
373 to compare relative grain-fabric differences between bed divisions in individual beds, as this may
374 yield information about the depositional conditions and syn-depositional shearing of the bed. It is
375 stressed that although the sample orientation is consistent for individual beds (parallel to bedding),
376 the orientation with respect to palaeoflow is constrained only by the overall orientation of Fan 3 (e.g.
377 Hodgson et al. 2006; Luthi et al. 2006; Prélat et al. 2009). Grain alignment is influenced by section
378 orientation with respect to palaeoflow, which potentially differed between divisions in individual
379 beds. Nevertheless, the approach gives some support to observations and inferences made in the
380 field, and provides a relative comparison between bed divisions, which is the principal utility here.
381 Long axes were recorded using an automated QEMSCAN® process, meaning that a large number of
382 samples can be analysed quickly (1-2 orders of magnitude more grain measurements than typical
383 manual thin-section fabric studies, e.g., Kane et al., 2010a).

384 Results:

385 With one exception, samples from hybrid beds show Von Mises type distributions (normal circular
386 distribution) with vectorial concentrations (K, a measure of mean vector strength) in the range of
387 0.17-0.75, with a mean value of $K = 0.5$. In contrast, turbidites are characterised by Von Mises and
388 uniform distributions, distributions with low K values, from 0.04-0.6 with a mean value of $K=0.26$
389 (Table 2 and Fig. 13).

390 *Interpretation:*

391 Hybrid beds have a strong grain orientation in comparison to the turbidites (Fig. 13); this fabric is
392 attributed to shearing within the cohesive flow. The low K values for the turbidites support their
393 origin as deposits from high-density turbidity currents where sediment deposition to the bed
394 precluded significant bedload transport or grain organisation. Deposits of low-density turbidity
395 currents, reported in a previous study by Kane et al. (2010a), have better organisation than these
396 deposits with Von Mises and Gaussian (non-circular) distributions, illustrating grain organisation by
397 tractional processes. The strong fabric reported for these hybrid beds suggests that the high-
398 concentration flows, to which they are attributed, were still relatively fluidal with internal shear
399 layers along which elongate grains are aligned.

400 *Stratigraphic and spatial distribution of bed types*

401 Typically, the Fan 3 stratigraphic succession is marked at its base by silty low-density turbidites,
402 which progressively thicken and coarsen upwards from fine siltstones to very-fine sandstones (Figs.
403 4 & 5). In some places, the first medium to thick beds occur abruptly at the base of the sandy part of
404 Fan 3, and are then overlain by several variably well-developed thickening- and coarsening-upward
405 packages, which are interpreted to represent the individual lobe deposits (Fig. 2). Bed thickness
406 patterns are, however, variable (Prélat and Hodgson, 2013). Fine-scale mapping and correlation by
407 Prélat et al. (2009) led to extensive thin-bedded successions being treated as distinct elements, and
408 were interpreted as the distal fringes of lobes (Prélat and Hodgson, 2013), implying a pronounced
409 compensational stacking pattern. Hybrid beds are found within the lower to middle part of the Fan 3
410 succession in the distal areas, and are interbedded with turbidites. Within the turbidite succession
411 described above the hybrid beds stack from the distal-, to medial to proximal lobe fringe types
412 described above (Figs. 4 & 5). Interbedded throughout the succession are packages of thin-bedded
413 sandstone and siltstone low-density turbidites. High-density turbidites, and thick-bedded turbidites of
414 uncertain affinity, are well developed in the feeder channel-fills, axial and off-axis areas of the lobes,
415 down-dip of scours and in association with channelised features developed across the lobes; they
416 generally occur at the top of individual lobe stratigraphic units, but can occur at their bases (Morris
417 et al., 2000; Johnson et al., 2001; Hodgson et al., 2006).

418 *Interpretation*

419 The character of flows passing over the Fan 3 lobes can be subdivided into turbidity currents, which
420 deposited a range of low- to high-density turbidites, and the higher concentration transitional or
421 laminar flows inferred above, which deposited hybrid beds. Low-density turbidites are common
422 across all environments and tend to increase in proportion and thin towards the distal pinch-out (e.g.,
423 Morris et al., 2000). The low concentration and relatively low degree of density stratification of the
424 flows allowed them to traverse gentle gradient changes associated with depositional relief across the
425 lobes (Groenenberg et al., 2010). High-density turbidites and transitional to laminar facies were
426 deposited by high-concentration flows, and appear to have been strongly controlled by topography
427 related to previous deposits (Groenenberg et al., 2010). High-density turbidites are related to the
428 main feeder channels and low-relief distributary channels developed across the lobe (e.g., Morris et
429 al., 2000; Johnson et al., 2001; Hodgson et al., 2006), and may be the expression of the flows that cut
430 major scours in the channel lobe transition zone (e.g., Hofstra et al., 2015). The flows that deposited

431 these facies are thought to have been strongly density stratified; as such, individual large magnitude
432 flows were able to make their own pathway(s) following depositional topography of precursor lobe
433 deposits and developing ‘finger-like’ bodies across the lobe (Groenenberg et al., 2010). Simple
434 trends of bed thickening associated with lobe progradation, which might be expected in the simplest
435 case (e.g., Mutti and Sonnino, 1981), are obscured by the juxtaposition of thicker beds marking
436 either the onset of a new lobe (but not always), or occurring apparently randomly within an
437 otherwise thickening (or thinning) upwards trend. Nevertheless, the hybrid beds are for the most part
438 associated with medial and distal lobe frontal fringe environments (cf. Spychala et al., in revision),
439 and are developed down-dip of high-density turbidites. Stratigraphically, therefore, the hybrid beds
440 typically occur in the basal parts of lobe successions (Hodgson, 2009). In addition, they can occur in
441 packages representing only the distal fringe of a lobe, i.e., in areas where the sandier parts of the lobe
442 did not reach (e.g., Log Sk4, Fig. 5). The point where transformation occurs is the subject of the
443 following section.

444

445 **Discussion**

446 **Fan 3 turbidity currents and flow transformation**

447 Whilst much of the Fan 3 stratigraphy is dominated by turbidites, sedimentary facies tracts and
448 stratigraphic stacking suggest that some turbidity currents transformed to transitional or laminar
449 flows (e.g. McCave & Jones, 1988; see review by Talling, 2013). This interpretation is based on the
450 downstream facies transitions described above, whereby turbidites pass downstream into hybrid
451 beds. The ability of a turbidity current to maintain sediment in suspension is affected by lateral
452 spreading and associated deceleration; we postulate that this alone can force local flow
453 transformation, resulting in deposition of a hybrid bed in the distal parts of a lobe.

454

455 The analysis utilises the suspension capacity parameter Γ (Eggenhuisen et al., 2016), a measure of a
456 flow’s ability to maintain sediment in suspension, in conjunction with a geometrical model of flow
457 expansion. A simple numerical model is developed to show how Γ evolves as a turbidity current
458 spreads laterally and decelerates across a lobe. In this discussion, a ‘lobe’ scale is used rather than a
459 ‘lobe element’ as the latter are less well-constrained. The suspension capacity parameter Γ represents
460 a force balance between the downward gravity force, F_g , and upward directed turbulent forces (F_{turb})
461 that can be used to compare dynamic turbulence scales to gravitational scales acting near the base of

462 turbidity currents. F_g is the net force resulting from buoyancy and gravity acting on sediment grains
463 in suspension. The turbulent force scale F_{turb} is derived from universal scaling of turbulent
464 Reynolds-stress gradients in the region just above the bed where turbulent structures are generated
465 that export excess turbulent kinetic energy that cannot be dissipated in the boundary layer upward
466 into the flow (Pope, 2000). This region will be a few millimetres to centimetres thick in a typical
467 turbidity current. The suspension capacity parameter Γ is given by (see Eggenhuisen et al. [2016] for
468 a full derivation):

$$470 \quad \Gamma = \frac{F_{turb}}{F_g} = \frac{u_*^3}{140\nu g R C_b} \quad (\text{Equation 1})$$

471
472 Where u_* is the shear velocity, ν is the kinematic viscosity of water ($1.002 \cdot 10^{-6} \text{ m}^2/\text{s}$), g is the
473 constant of acceleration by gravity, C_b is volumetric sediment concentration near the bed, and
474 $R = (\rho_s - \rho_f)/\rho_f$ is the relative density of sediment where ρ_s and ρ_f are the particle and fluid
475 density respectively (2650 kg m^{-3} for quartz and 1020 kg m^{-3} for seawater) giving $R = 1.6$. The
476 numerical constant 140 derives from universal scales of vertical turbulence in boundary layer flow
477 (Eggenhuisen et al., 2016).

478 Near-bed turbulence dominates suspension when $\Gamma > 1$, and the turbulent conditions could maintain
479 more sediment in suspension, such that, additional sediment can be entrained into the passing flow if
480 it is readily available at the bed. This condition is therefore termed under-saturated with respect to
481 the turbulent suspension capacity of the flow. At $\Gamma = 1$, turbulent forces near the bed are equal to the
482 gravitational pull on the suspended particle load. This force balance prevents average net vertical
483 acceleration of the sediment particles and the fluid between them, and the flow is in saturation
484 equilibrium with suspended sediment near the boundary; in this condition C_b can be seen as a
485 saturation concentration.

486 Gravity dominates suspension when $\Gamma < 1$ and the upward turbulent forces are smaller than
487 downward gravitational forces applied to the fluid by the particles, this prevents turbulent
488 accelerations and results in turbulence extinction. This condition is termed over-saturated with
489 suspended sediment because the flow does not have sufficient turbulent capacity to suspend all the
490 particles present near the bed. A recent breakthrough in DNS simulations of turbidity currents
491 (Cantero et al., 2009, 2011, 2012) demonstrates how turbulence production at the base of turbidity

492 currents is shut-down rapidly in over-saturated suspensions, leading to rapid laminarization
 493 extending upwards in the flow. The result will be increasing sediment stratification towards the base
 494 of flow as there is no mechanism to counter the gravitational settling of sediment. A key outcome of
 495 the work by Cantero et al. (2009, 2011, 2012) and Eggenhuisen et al. (2016) is that extinction of
 496 turbulence can occur at very low absolute concentrations of suspended sediment. The conventional
 497 perception that turbulence suppression occurs at high sediment concentrations is only true in very
 498 high energy flows. Low concentrations suffice to fully suppress turbulence generation in moderate or
 499 gentle flow conditions. Occurrence of hindered settling at sufficiently high sediment concentrations
 500 can slow down and delay sediment accumulation rates to the base of the flow, but cannot stop
 501 sediment in a laminarized flow from settling completely.

502 Equation 1 is coupled to a model describing the structure of an oversaturated turbidity current
 503 spreading over a lobe, after exiting a channel mouth to investigate the evolution of Γ in the spreading
 504 flow. Estimation of the suspension capacity parameter depends on an estimation of the shear velocity
 505 from the flow scales:

$$506 \quad u^* = \sqrt{gH\bar{C}RS} \quad (\text{Equation 2})$$

507 Where \bar{C} is the depth averaged concentration, H is the flow thickness [m] (see discussion below),
 508 and S is the tangent of the slope [-]. in the model output, the turbidity current exiting the channel is
 509 followed while it spreads out over the lobe. The flow is considered uniform, and its bulk discharge is
 510 conserved, such that the product of depth averaged flow velocity, flow thickness, and flow width W
 511 is constant as the current travels in direction x along the lobe:

$$512 \quad Q_b = H(x)\overline{U(x)}W(x) = \text{constant} \quad (\text{Equation 3})$$

513 A drag coefficient C^d is used to set a fixed ratio between the average velocity and shear velocity:

$$514 \quad C^d = U/u^* \quad (\text{Equation 4})$$

515 The value of the drag coefficient C^d is set to 0.005 (following Parker et al., 1987). Essentially, this
 516 model describes a depth averaged flow structure at different positions during passage over a lobe
 517 assuming that friction always balances gravitational driving force. The different positions are linked
 518 by the volumetric requirement that all discharge debauched from the input condition of the channel
 519 mouth is spread equally over the lobe surface by lateral spreading, not by consideration of energy in
 520 the form of momentum changes, potential energy losses, or variations in the budget of turbulent

521 kinematic energy. This analysis is thus cruder than depth averaged simulations that solve such
522 energy equations. The purposeful simplicity of this model makes the system easy to investigate and
523 robust to the interrogation of first order controls on the flow structure with distance.

524 The main simplifying assumptions on the behaviour of the turbidity current are: there is no erosion
525 or deposition as source or sink terms in Eq. 3 (constant discharge). Slope gradient is constant, not
526 some decreasing function $S(x)$ of along-lobe distance x . The drag coefficient is constant in Eq. 4,
527 and does not change with changing friction against the ambient water. The flow spreads out equally
528 over the lobe surface, and does not focus in preferential flow pathways. The model predicts both
529 when turbulence is damped and when the flow collapses but does not model the movement and
530 character of dense layers that then form. The effect of these simplifying assumptions will be
531 discussed following the main result.

532 The discharge can be expressed purely as a function of the flow geometry by substituting Eq.4 and
533 Eq.2 into Eq.3:

$$534 \quad Q_b = \frac{\sqrt{g \overline{CRS}}}{\sqrt{C_d}} H(x)^{1.5} W(x) \quad (\text{Equation 5})$$

535 The geometries of the channel deposits in the proximal areas of Fan 3 are used to constrain the flow
536 dimensions that fed from channels onto the lobe surfaces. Channel depth (h) is used as a proxy for
537 flow thickness (H); in Fan 3, channel depths (in the proximal parts of the stratigraphy) are in the
538 range of 5-13 m (e.g. Sullivan et al. 2000, from the Ongeluks River outcrops). This approach
539 provides a minimum value for flow thickness (e.g., El-Gawad et al., 2012) as flows may be
540 significantly super-elevated above the channel depth (e.g., Piper & Normark, 1983, Mohrig &
541 Buttles, 2007, Kane et al., 2010b), however, it is assumed that the channel depth values are within
542 the same order of magnitude as the original flow thickness. In a series of physical experiments,
543 Mohrig & Buttles (2007) demonstrated that over-spilling (super-elevated) channelized turbidity
544 current thicknesses were typically in the range of $h/H \leq 1.3$. The relationship of channel fill
545 thickness to instantaneous channel depth is also not straightforward, but if we assume a minimum
546 depth of 13 m (maximum channel fill thickness) then, if $h/H \leq 1.3$, we have a minimum estimate of
547 $H=17$ m at the lobe apex (i.e., channel to lobe transition area), negating burial compaction effects.
548 Groenenberg et al. (2010) estimated a thickness of 4 m based on the height of depositional relief in
549 the medial to distal parts of the lobe. Lobe width ($W=15$ km) is used as a proxy for the maximum
550 flow width and lobe length is taken as 25 km (Prélat et al., 2009). The flow is assumed to spread

551 evenly over the full width of the surface of the lobe, and the width is set to increase linearly from the
552 width of the channel at the lobe apex (250 m) to the full lobe width at a distance similar to the lobe
553 length. The evolution of flow thickness, flow velocity, and shear velocity with distance along the
554 lobe can now be resolved using these assumptions (Fig.16). Flow thickness is equal to the estimate
555 from channel depth at the lobe apex (17 m) and decreases rapidly proximally from 0-5 km to about 4
556 m thick (corresponding approximately to the values estimated by Groenenberg et al. 2010 for the
557 medial–distal lobe), and more slowly to the lobe termination at 25 km. Flow velocity and shear
558 velocity show similar patterns (Fig. 16B). The evolution of the suspension capacity parameter, Γ ,
559 goes through the threshold value of 1, at which point turbulence is suppressed at 21km from the lobe
560 apex and 4 km from lobe pinch-out (Fig. 16C).

561

562 **Discussion of the numerical model**

563 The model demonstrates that a laterally spreading turbidity current, without entrainment of eroded
564 substrate material (or water), will decelerate, thin and lose its suspension capacity as the bed shear
565 velocity decreases. The model is necessarily simple as there are many poorly constrained parameters
566 and spatially variable feedbacks that may obscure the analysis of the first order parameters
567 governing suspension capacity. However, whilst inclusion of such second order effects in the
568 equations presented would modify the predicted flow conditions for the estimated values of slope
569 and channel mouth concentration, and thereby the loci of the flow transformation, the first order
570 result that flow spreading can result in flow transformation in the distal sections of lobes remains.
571 Previous models have suggested flow collapse in a similar manner, but are reliant on the poorly
572 constrained gradient Richardson number (e.g. McCave and Jones, 1988) or the shear Richardson and
573 shear Reynolds numbers (e.g., Cantero et al., 2012). These approaches necessitate the incorporation
574 of grain-size and settling velocity to establish vertical gradients of velocity and concentration, and
575 are dependent on bulk-flow Reynolds numbers. The present model avoids these ambiguities.

576 The model presented above infers a homogenous and steady longitudinal flow structure, but it can be
577 envisaged that Γ varies spatially within the flow, as well as temporally as demonstrated. This is a
578 necessary simplification for the purposes of this discussion. The overall lobe body is by definition a
579 depositional unit; if the suspension capacity parameter sets deposition this would imply that $\Gamma = 1$ is
580 at the lobe apex/channel mouth. This may be explained by the longitudinal structure of the flows,
581 and the general trend of progradation through time, such that successive flows tend to step farther

582 basin-ward during the growth phase; this may include the precise position of the channel-lobe
583 transition and lobe apex (e.g., Hodgson et al., 2016; de Leeuw et al., 2016).

584 The longitudinal structure of the flows in terms of Γ may be expressed by the vertical facies
585 stacks in individual lobes. In proximal areas erosion surfaces overlain by relatively clean basal
586 sandstones may indicate that $\Gamma > 1$ during the passage of the head and body, switching to $\Gamma \leq 1$ during
587 deposition of the tail-end of the flow. Distally, muddy sandstones overly conformable bed bases,
588 have a high matrix content and display sheared fabrics, suggesting that basal flow was laminar from
589 the onset at its arrival at distal locations, i.e., $\Gamma < 1$.

590 The implication of the observed erosion in the proximal lobes suggests that flows exiting the
591 channel mouth were under-saturated ($\Gamma > 1$) but may also be diagnostic of bathymetric control on
592 flow behaviour at the confined-to- unconfined transition, e.g., a hydraulic jump. The purposeful
593 simplicity of the model has the benefit that the effects of the main simplifications can be isolated and
594 analysed.

595 *Erosion and deposition.*

596 The outcrops show evidence for erosion in proximal lobe locations, indicating that material was
597 entrained in the first few to 10 km after a flow exited the channel. Erosion would increase flow
598 volume, concentration and/or thickness, flow velocity, and bed-shear velocity in the proximal
599 section of the lobe to values exceeding those of the scenarios presented in Figures 17 and 18, and
600 thereby delay flow transformation. Deposition of sediment from the laminarised base of the flow
601 down-dip of flow transformation will decrease the amount of sediment in suspension, and thereby
602 bed shear stress, leading to inevitable collapse of the flow. Thus, erosion then deposition can cause
603 the flow transformation point to be located in more distal positions than those indicated by Figures
604 17 and 18, but would not alter the result that flow spreading is sufficient to force transition to
605 deposition from laminarised flow.

606 *Constant slope.*

607 Slope gradient is a main control on sediment bypass (Stevenson et al., 2015), and bypass-dominated
608 channels tend to form on gradients that are relatively steeper, whilst deposition-dominated lobes tend
609 to form on slopes that are relatively more gentle (e.g., Kneller, 2003). This decrease in slope is not
610 incorporated into the analysis presented above. In addition, the surface is assumed to be smooth
611 whilst in reality a complex topography of older lobe deposits and basin relief will affect the flows

612 (Prélat et al., 2009; Groenenberg et al., 2010; Spychala et al., 2016). Down-dip decrease in slope is
613 expected to decrease the flow capacity over the proximal lobe more rapidly than illustrated in the
614 scenarios of Figures 16 and 17. In addition, aggradational and erosional relief will introduce lateral
615 flow variability and lateral stacking variability (Prélat et al., 2009; Groenenberg et al., 2010).

616 *Constant drag coefficient.*

617 The ratio between drag at the upper surface and the bed on turbidity currents is recognised to vary
618 based on flow conditions (e.g., Parker et al., 1987; Sequeiros, 2012). However, the shift in relative
619 drag is commonly ignored in analyses, as it has been here. At low Richardson scales, mixing at the
620 top of the turbidity current is reduced, which reduces friction at the top when compared to friction at
621 the base of the flow (Kneller et al., in review). This balance is assumed to be constant in the usage of
622 Eq. 4. The bed shear stress is still decreasing monotonically with distance along the lobe, but at a
623 lower rate than the scenarios presented in Figures 16 and 17 when the balance of friction is allowed
624 to shift towards the bed with lower Richardson scales. The effect of this phenomenon is the delay of
625 flow transformation to a more distal location.

626 *Equal spreading over the lobe.*

627 The observed finger-like geometry of Fan 3 and the associated facies distribution is evidence for
628 focussed flow pathways (Rozman 2000; Rozman and Bouma 2000; Johnson et al., 2001; Hodgson et
629 al., 2006; Groenenberg et al., 2010). Consequently, the flow does not cover the lobe equally and
630 flow capacity will be higher along the pathways due to the higher amounts of sediment in
631 suspension, and increased flow velocity increasing the basal shear velocity. On the fringes of these
632 pathways it may be possible that lateral flow may undergo transformations (Spychala et al., in
633 revision).

634

635 **Flow transformation**

636

637 Reduction in the flow suspension capacity as described above may lead to the development of a
638 dense, cohesive lower boundary layer flow, where flows are primed to do so (abundance of clay
639 minerals and fine grained sediment). A steady, non-cohesive, low concentration turbidity current has
640 a given capacity, which drops as the flow decelerates (Hiscott, 1994). Accordingly, sediment falls
641 from suspension to the bed to form a grain framework, or 'rigid' bed which may or may not be

642 reworked depending upon the shear stress exerted by the flow on the bed. Sediment suspensions with
643 a significant cohesive and very fine-grained fraction behave differently and have the potential to
644 form fluid beds due to the high water content of clay floccs and fluid trapping by very fine-grained
645 non-cohesive sediment, which may allow the ‘bed’ to continue to flow (e.g., Winterwerp & Van
646 Kesteren, 2004). Silt and very fine sand may settle into the dense basal layer together with larger
647 clay floccs and other relatively large clasts and grains (mud clasts, micas, organic material). The
648 aggrading dense boundary layer flow, developed in the decelerating and progressively more
649 stratified flow, would therefore be saturated and cohesive, and given the appropriate conditions,
650 would be able to continue flowing downstream as a cohesive flow (rather than settling to form a
651 rigid bed). In such a flow, yield strength and buoyancy may become the primary particle support
652 mechanisms (e.g., Talling, 2013). McCave and Jones (1988) suggest that under these conditions
653 shearing at the lower boundary layer and continuous flux of the ambient fluid may flush the dense
654 lower layer breaking up clay floccs and pushing clay upwards in the flow or mobile deposit. This may
655 give rise to the development of a slightly better sorted thin lower layer, upon which the clay rich
656 suspension rides; and may explain the thin slightly better sorted layer present at the base of most of
657 the hybrid beds deposits documented here. Support for this comes from the presence of mud clasts
658 along intra-bed boundaries between basal relatively clean sandstone and overlying muddier
659 sandstones (e.g. Fig. 7E), suggesting that relative particle buoyancy may have played a role in the
660 lowermost part of the flow; in addition, sand may have settled from the overriding plug flow (e.g.,
661 Sumner et al., 2009).

662
663

664 The minimum yield strength (τ_y) required to support a given grain size (d_{max}) within the inferred
665 transitional to laminar flows can be calculated, following Johnson (1970) and Hampton (1972,
666 1975):

$$d_{max} = \frac{8.4\tau_y}{(\rho_p - \rho_f)g}$$

667 (8)

668 Hampton (1972) demonstrated that this was a reliable approximation for sand particles submerged in
669 a clay-water matrix. To maintain laminar support of 125 μm quartz grains, that equates to a low
670 yield strength, 0.2 Pa. Flow concentrations in the range of 6% kaolin clay would be required to

671 generate the necessary yield strength to support 125 μm quartz grains; concentration is calculated by
672 rearranging Wan's (1982) formula:

$$\tau_y = 1280 \left(\frac{C}{100} \right)^3$$

673 (9)

674 The empirical formulation of Wan (1982) is only valid for kaolin flows, however, the petrological
675 analysis suggests that the primary clay was most-likely illite, which tends to form stronger bonds
676 than kaolin (see mineralogy section above). Shearing intensity decreases yield strength considerably
677 (Hampton, 1975), therefore the effect of shear stress on these flows also needs to be considered. For
678 example, Sumner et al. (2009) found that concentrations of approximately 14% kaolin were needed
679 to support very fine- to medium-grained sand (63-250 μm) in shearing clay-rich flows; similar
680 figures were suggested from the settling tube experiments of Amy et al. (2006). Additionally, Major
681 and Pierson (1992), in a series of experiments on sand-silt-clay slurries, noted that small changes in
682 sediment concentration, in the order of 2-4%, produced yield strength changes of up to an order of
683 magnitude. The minimum concentration estimate above (6% clay) is within the range of flow
684 concentrations considered by McCave & Jones (1988) (5-10%) for the generation of clay-silt yield
685 strength dominated flows; however the values of Sumner et al. (2009) (~14% clay; albeit kaolin) for
686 shearing fine-sand bearing flows are probably more appropriate.

687 The advection distance of these flows appears to be in the order of several kilometers, based
688 on bed length, suggesting that dewatering was a relatively slow process. Assuming that the laminar
689 flows initially have the flow velocity of their parent turbidity currents, e.g., for a 5% concentration
690 flow this might be in the region of 0.4 m/s (Figure. 16B), an advection distance of 4 km (from the 21
691 km 'transformation point' to the lobe pinch-out) would suggest a dewatering time of c. 2.5 hours. In
692 all likelihood, the average flow velocity is significantly lower. A 0.2 m/s flow would suggest a
693 dewatering time of 5 hours; dewatering times are anticipated to be significantly longer for flows with
694 clays forming stronger bonds. There is much local variability, which likely reflects subtle changes in
695 gradient and orientation with respect to palaeoflow.

696

697 **Summary and comparison to 'long-distance transformation model'**

698 The Fan 3 hybrid beds are related to events that entrained the substrate. Radial spreading of
699 individual flows and consequent deceleration caused the flow suspension capacity to be overcome,
700 and flows became transitional to laminar. Due to the high proportion of cohesive and fine material, a
701 dense low yield strength flowing layer formed, which progressively shut off the transfer of turbulent
702 kinetic energy from the base of the flow into the upper layers. Following this, the flows rapidly lost
703 energy and consequently come to a rest relatively abruptly, with the cleaner-lower and muddier-
704 upper deposits pinching out approximately contemporaneously. The transformation model is broadly
705 similar to that postulated by McCave and Jones (1988), and Talling's (2013) model 3. The principal
706 difference to Hodgson's (2009) 'D2' model is that the basal sandstones are here not considered to be
707 the product of forerunning turbidity currents, rather they are considered to be the product of distal
708 flow collapse and transformation, although both models rely on incorporation of substrate material
709 updip. As demonstrated by the numerical model, deceleration alone may result in flow
710 transformation (Model 3 of Talling, 2013), but in this case the evidence shows that many of the
711 flows depositing hybrid beds behaved erosively updip when they were undersaturated ($\Gamma > 1$), and
712 through deceleration became saturated ($\Gamma < 1$) and transformed to transitional-laminar flows.

713 Transformation appears to be a general characteristic of decelerating clay-rich flows (Talling, 2013).
714 If the coarser fraction of the flow has not completely settled at the point where viscous forces begin
715 to dominate, these grains will be incorporated into the higher strength flow (Talling, 2013). In the
716 case of the style of distal beds outlined here, and seen elsewhere in systems of a similar grain size,
717 (e.g. the Wilcox Fm. Zarra et al., 2007; Kane & Pontén, 2012), the low settling velocity of the very
718 fine-grained sand and coarse silt, may make these type of deposits common. This is for two reasons:
719 1) coarser grained flows may undergo sedimentation earlier, without time for the transformation to
720 occur; 2) coarser or denser grains require greater turbulent energy to be supported, and this may
721 inhibit the formation of clay bonds. Consequently, in coarser-grained systems lacking the fine tail,
722 these types of hybrid beds may not develop.

723

724 **Conclusions**

725 Sedimentary facies in the distal parts of deep-marine lobes are shown to differ significantly from
726 those predicted by classical models; this has important implications for palaeo-environmental
727 interpretations and facies predictions. A downstream transition from turbidite-dominated
728 stratigraphy to mixed turbidites and hybrid beds is documented. Hybrid beds from the distal parts of

729 Fan 3 stratigraphy are characterised and placed within a physical model based on application of the
730 suspension capacity parameter, Γ . Flow transformation is inferred to take place through:

- 731 1. Erosion and entrainment by turbidity currents of clay, silt and very fine sand in the
732 channel to channel-lobe transition zone areas when flows are undersaturated ($\Gamma > 1$)
733
- 734 2. Deceleration of flows is associated with radial spreading from the lobe apex, reduction in
735 bed shear stress and accordingly a reduction in suspension capacity; we present a simple
736 model for estimation of this.
737
- 738 3. Formation of a low yield-strength cohesive basal layer, which flows in a transitional to
739 increasingly laminar manner that allows settling of the denser/coarser grained fraction.
740
- 741 4. The rising yield strength of the lower layer inhibits the efficiency of vertical mixing,
742 leading to a collapse of the turbulent energy field and en-masse transformation of the
743 upper part of the flow. This results in a thick argillaceous sandstone division containing
744 the residual material within the flow (sand, silt, clay, organics, mica grains).

745

746 Flow transformation is primed by erosion of substrate material within the feeder channels and
747 proximal parts of the lobe; laminarization and the deposition of hybrid beds occurs farther down-dip
748 in response to flow expansion and deceleration. The fine-grained nature of the Fan 3 gravity flow
749 system may have promoted the development of these types of flows, with the fine suspended load
750 transforming to low yield-strength driven flows following loss of suspension capacity; this is
751 potentially the reason that very similar facies are found in other systems of similar grain size range
752 (e.g., Ross Fm., e.g., Pyles & Jennette. (2009), Wilcox Fm., e.g., Zarra (2007)).

753 **Acknowledgements**

754 This research was made possible with the logistical assistance of Steve Flint, Deville Wickens and
755 the staff of Inverdoorn Game Reserve, for which we are grateful. Numerous colleagues at Statoil
756 have given assistance, support and advice in the field and planning stages: Lars-Magnus Fält, Frode
757 Hadler-Jacobsen, Nils Erik Janbu, Stephen Johnson and Carlo Messina are all thanked. Ruth Elin
758 Midtbø is thanked for the thin-section photographs. Zoltan Sylvester is thanked for comments on an
759 earlier version of this manuscript; Peter Haughton, Mauricio Perillo and in particular Associate

760 Editor Peter Talling are thanked for their thoughtful reviews and for guidance which greatly
761 improved the manuscript.

762

763 **References**

764 **Amy, L.A. and Talling, P.J.** (2006) Anatomy of turbidites and linked debrites based on long
765 distance (120 × 30 km) bed correlation, Marnoso Arenacea Formation, Northern Apennines, Italy.
766 *Sedimentology*, **53**, 161-213.

767

768 **Amy, L.A., Talling, P.J., Edmonds, V.O., Sumner, E.J. and Lesueur, A.** (2006) An experimental
769 investigation of sand–mud suspension settling behaviour: implications for bimodal mud contents of
770 submarine flow deposits. *Sedimentology*, **53**, 1411–1434.

771

772 **Baas, J.H., Hailwood, E.A., McCaffrey, W.D., Kay, M., and Jones, R.** (2007) Directional
773 petrological characterisation of deep-marine sandstones using grain fabric and permeability
774 anisotropy: methodologies, theory, application and suggestions for integration. *Earth-Science*
775 *Reviews*, **82**, 101–142.

776

777 **Baas, J.H., Best, J.L., Peakall, J., and Wang, M.** (2009) A phase diagram for turbulent,
778 transitional and laminar clay suspension flows. *Journal of Sedimentary Research*, **79**, 162–183,
779 doi:10.2110/jsr.2009.025.

780

781 **Baas, J.H., Best, J.L., and Peakall, J.** (2011) Depositional processes, bedform development and
782 hybrid bed formation in rapidly decelerated cohesive (mud–sand) sediment flows. *Sedimentology*,
783 **58**, 1953–1987. doi:10.1111/j.1365-3091.2011.01247.x.

784

785

786 **Barker, S.P., Haughton, P.D.W., McCaffrey, W.D., Archer, S.G., and Hakes, B.** (2008)
787 Development of rheological heterogeneity in clay-rich high-density turbidity currents: Aptian
788 Britannia Sandstone Member, U.K. Continental shelf. *Journal of Sedimentary Research*, **78**, 45–68,
789 doi:10.2110/jsr.2008.014.

790
791 **Bouma, A.H.** (1962) *Sedimentology of some flysch deposits: A graphic approach to facies*
792 *interpretation*. Elsevier, Amsterdam, 168 pp.
793
794 **Bouma, A.H. and Wickens, H.D.** (1991) Permian passive margin submarine fan complex, Karoo
795 Basin, South-Africa: possible model to Gulf of Mexico. *Transactions-Gulf Coast Association of*
796 *Geological Societies*, **41**, 30-42.
797
798 **Cantero, M. I., Balachandar, S. and Parker, G.** (2009), Direct numerical simulation of
799 stratification effects in a sediment- laden turbulent channel flow, *Journal of Turbulence*, 10, 37–41.
800
801 **Cantero, M.I., Cantelli, A., Pirmez, C., Balachandar, S., Mohrig, D., Hickson, T.A., Yeh, T-H.,**
802 **Naruse, H. and Parker, G.** (2012) Emplacement of massive turbidites linked to extinction of
803 turbulence in turbidity currents. *Nature Geoscience*, **5**, 42-45.
804
805 **Cantero, M. I., Shringarpure, M. and Balachandar, S.** (2012), Towards a universal criteria for
806 turbulence suppression in dilute turbidity currents with non-cohesive sediments. *Geophysical*
807 *Research Letters*, **39**, L14603.
808
809 **Cole, D.I.** (1992) Evolution and Development of the Karoo Basin. *Inversion Tectonics of the Cape*
810 *Fold Belt, Karoo and Cretaceous Basins of Southern Africa*, 87-99.
811
812 **Coulson, J.M. and Richardson, J.F.** (1991) Chemical Engineering Vol. 2. Butterworth Heinemann,
813 Oxford. 1183p.
814
815 **Dapples, E.C., and Rominger, J.F.** (1945) Orientation analysis of fine-grained clastic sediments: a
816 report of progress. *Journal of Geology*, **53**, 246–261.
817
818 **DeCelles, P.G. and Giles, K.A.** (1996) Foreland basin systems. *Basin Research*, **8**, 105-123.
819
820 **De Leeuw, J., Eggenhuisen J.T. and Cartigny, M.J.B.** (2016) Morphodynamics of submarine
821 channel inception revealed by new experimental approach. *Nature Communication*, **7**:10886 doi:
822 10.1038/ncomms10886

823 **De Wit, M.J., and Ransome, I.G.D.** (1992) Regional inversion tectonics along the southern margin
824 of Gondwana. In: Inversion Tectonics of the Cape Fold Belt, Karoo and Cretaceous Basins of
825 Southern Africa. In De Wit, M.J., and Ransome, I.G.D. Rotterdam, Balkema, p. 15–21.
826

827 **El-Gawad, S. Abd., Cantelli, A., Pirmez, C., Minisini, D., Sylvester, Z. and Imran, J.** (2012)
828 Three-dimensional numerical simulation of turbidity currents in a submarine channel on the seafloor
829 of the Niger Delta slope. *Journal of Geophysical Research*, 117, C05026.
830

831 **Eggenhuisen, J.T., Cartigny, M.J.B. and de Leeuw, J.** (2016). Physical theory for near-bed
832 turbulent particle-suspension capacity. *Earth Surface Dynamics Discussion*, doi:10.5194/esurf-2016-
833 33.
834

835 **Fildani A., Weislogel A., Drinkwater N.J., McHargue T., Tankard A., Wooden J., Hodgson D.,**
836 **Flint S.** (2009) U-Pb zircon ages from the southwestern Karoo Basin, South Africa—Implications
837 for the Permian-Triassic boundary. *Geology*, **37**, 719–722. doi: 10.1130/G25685A.1.
838

839 **Fildani, A., Weislogel, A., Drinkwater, N.J., McHargue, T., Tankard, A., Wooden, J., Hodgson,**
840 **D. and Flint, S.** (2009) U-Pb zircon ages from the southwestern Karoo Basin, South Africa-
841 Implications for the Permian-Triassic boundary. *Geology*, **37**, 719-722.
842

843 **Folk, R.L., Andrews, P.B. and Lewis, D.W.** (1974) Detrital sedimentary rock classification and
844 nomenclature for use in New Zealand. *New Zealand Journal of Geology and Geophysics*, **13**, 937-
845 968.
846

847 **Fonnesu, M., Haughton, P., Felletti, F., and McCaffrey, W.** (2015) Short length-scale variability
848 of hybrid event beds and its applied significance. *Marine and Petroleum Geology*, **67**, 583-603.
849

850 **Goldhammer, R.K., Wickens, H.DeV., Bouma, A.H., and Wach, G.** (2000) Sequence
851 stratigraphic architecture of the Late Permian Tanqua submarine fan complex, Karoo Basin, South
852 Africa, in Bouma, A.H., and Stone, C.G., eds., *Fine-Grained Turbidite Systems: American*
853 *Association of Petroleum Geologists, Memoir 72, and SEPM, Special Publication 68*, p. 165–172.
854

855 **Groenenberg, R.M., Hodgson, D.M., Prelat, A., Luthi, S.M. and Flint, S.S.** (2010) Flow-Deposit
856 Interaction in Submarine Lobes: Insights from Outcrop Observations and Realizations of a Process-
857 Based Numerical Model. *Journal of Sedimentary Research*, **80**, 252-267.

858

859 **Grundvåg, S.A., Johannessen, E.P., Helland-Hansen, W. and Plink-Björklund, P.** (2014)
860 Depositional architecture and evolution of progradationally stacked lobe complexes in the Eocene
861 Central Basin of Spitsbergen. *Sedimentology*, **61**, 535-569.

862 **Hampton, M.A.** (1972) The role of subaqueous debris flow in generating turbidity currents. *Journal*
863 *of Sedimentary Petrology*, **42**, 775–793.

864

865 **Hampton, M.A.** (1975) Competence of fine grained debris flows. *Journal of Sedimentary Petrology*,
866 **45**, 833–844.

867

868 **Haughton, P.D.W., Barker, S.P. and McCaffrey, W.D.** (2003) 'Linked' debrites in sand-rich
869 turbidite systems - origin and significance. *Sedimentology*, **50**, 459-482.

870

871 **Haughton, P., Davis, C., McCaffrey, W. and Barker, S.** (2009) Hybrid sediment gravity flow
872 deposits - Classification, origin and significance. *Marine and Petroleum Geology*, **26**, 1900-1918.

873

874 **Hiscott, R.N., and Middleton, G.V.** (1980) Fabric of coarse deep-water sandstones, Tourelle
875 Formation, Quebec, Canada: *Journal of Sedimentary Petrology*, **50**, 703–722.

876

877 **Hiscott, R.N.** (1994) Loss of capacity, not competence, as the fundamental process governing
878 deposition from turbidity currents. *Journal of Sedimentary Research*, **A64**, 209–214.

879

880 **Hodgson, D., Flint, S.S., Hodgetts, D., Drinkwater, N.J., Johannessen, E.P. and Luthi, S.M.**
881 (2006) Stratigraphic evolution of fine-grained submarine fan systems, Tanqua depocenter, Karoo
882 Basin, South Africa. *Journal of Sedimentary Research*, **76**, 20-40.

883

884 **Hodgson, D.** (2009) Distribution and origin of hybrid beds in sand-rich submarine fans of the
885 Tanqua depocentre, Karoo Basin, South Africa. *Marine and Petroleum Geology*, **26**, 1940–1956,
886 doi:10.1016/j.marpetgeo.2009.02.011.

887

888 **Hodgson, D., Kane, I., Flint, S., Brunt, R., Ortiz-Karpf, A.** (2016). Time transgressive
889 confinement on the slope and the progradation of basin-floor fans: Implications for the sequence
890 stratigraphy of deep-water deposits. *Journal of Sedimentary Research*, 86, 73-86.

891

892 **Hofstra, M. Hodgson, D.M. Peakall, J.; Flint, S.S.** (2015) Giant scour-fills in ancient channel-lobe
893 transition zones: Formative processes and depositional architecture. *Sedimentary Geology*, Volume
894 329, 98-114.

895

896 **Ito, M.** (2008) Downfan transformation from turbidity currents to debris flows at a
897 channel-to-lobe transitional zone: the lower Pleistocene Otadai Formation, Boso Peninsula, Japan.
898 *Journal of Sedimentary Research*, **78**, 668–682.

899

900 **Johnson, A.** (1970) *Physical Processes in Geology*, W. H. Freeman, New York. 577 p.

901

902 **Johnson, M.R.** (1994) Thin section grain size analysis revisited. *Sedimentology*, **41**, 985–999.

903

904 **Johnson, S.D., Flint, S., Hinds, D. and Wickens, H.D.** (2001) Anatomy, geometry and sequence
905 stratigraphy of basin floor to slope turbidite systems, Tanqua Karoo, South Africa. *Sedimentology*,
906 **48**, 987-1024.

907

908 **Kane, I.A., McCaffrey, W.D., and Peakall, J.** (2010a) On the origin of palaeocurrent complexity
909 within deep marine channel levees. *Journal of sedimentary Research*, **80**, 54-66.

910

911 **Kane, I.A., McCaffrey, W.D., Peakall, J. and Kneller, B.C.** (2010b). Submarine channel levee
912 shape and sediment waves from physical experiments. *Sedimentary Geology*, 223, 75-85.

913

914 **Kane, I.A. and Pontén, A.S.M.** (2012) Submarine transitional flow deposits in the Paleogene Gulf
915 of Mexico. *Geology*, **40**, 1119-1122.

916

917 **Khelifa, A. and Hill, P.S.** (2006) Models for effective density and settling velocity of clay flocs.
918 *Journal of Hydraulic Research*, **44**, 390-401.

919

920 **King, R.C.** (2005) *Structural evolution of the Cape Fold Belt; implications for sediment routing to*
921 *the SW Karoo Basin*, University of Liverpool, Unpublished, 327 pp.
922

923 **King, R.C., Hodgson, D.M., Flint, S.S., Potts, G.J. and Van Lente, B.** (2009) Development of
924 subaqueous fold belt as a control on the timing and distribution of deepwater sedimentation: An
925 example from the Southwest Karoo Basin, South Africa. In: Kneller, B., Martinsen, O.J., McCaffrey,
926 B. (Eds.), *External Controls on Deep-Water Depositional Systems. SEPM Special Publication*, **92**,
927 261-278.
928

929 **Kneller, B. C.** (1995) Beyond the turbidite paradigm: physical models for deposition of turbidites
930 and their implications for reservoir potential. In: *Characterization of Deep Marine Systems* (Eds A.J.
931 Hartley and D.J. Prosser), *Geol. Soc. Spec. Publ.*, **94**, 31–49.
932

933 **Kneller, B.C.** 2003. The influence of flow parameters on turbidite slope channel architecture.
934 *Marine and Petroleum Geology*, **20**, 901–910.
935

936 **López-Gamundí and Rossello, E.A.** (1998) Basin fill evolution and paleotectonic patterns along
937 the Samfrau geosyncline: the Sauce Grande basin–Ventana foldbelt (Argentina) and Karoo basin–
938 Cape foldbelt (South Africa) revisited. *Geologische Rundschau* **86**, 819-934.
939

940 **Lowe, D.R.** (1982) Sediment gravity flows: II. Depositional models with special reference to the
941 deposits of high-density turbidity currents. *Journal of Sedimentary Petrology*, **52**, 279-297.
942

943 **Lowe, D.R. and Guy, M.** (2000) Slurry-flow deposits in the Britannia Formation (Lower
944 Cretaceous), North Sea: a new perspective on the turbidity current and debris flow problem.
945 *Sedimentology*, **47**, 31-70.
946

947 **Luthi, S.M., Hodgson, D.M., Geel, C.R., Flint, S.S., Goedbloed, J.W., Drinkwater, N.J.,**
948 **Johanessen, E.P.** (2006) Contribution of research borehole data to modelling fine-grained turbidite
949 reservoir analogues, Permian Tanqua-Karoo basin floor fans (South Africa). *Petroleum Geology*, **12**,
950 175–190.
951

- 952 **McCave, I.N. and Jones, K.P.N.** (1988) Deposition of ungraded muds from high-density non-
953 turbulent turbidity currents. *Nature*, **133**, 250-252.
- 954
- 955 **Major, J.J. and Pierson, T.C.** (1992) Debris Flow Rheology: Experimental analysis of fine-grained
956 slurries. *Water Resources Research*, **28**, 841-857.
- 957
- 958 **Martinsen, O. J., T. Lien, and R. G. Walker** (2000) Upper Carboniferous deep water sediments,
959 western Ireland: analogues for passive margin turbidite plays, in P. Weimer, R. M. Slatt, J. Coleman,
960 N. C. Rossen, H. Nelson, A. H. Bouma, M. J. Styzen, and D. T. Lawrence, eds., Deep-water
961 reservoirs of the world, Gulf Coast Section-SEPM Special Publication, p. 533-555.
- 962
- 963 **McKay, M.P., Weislogel, A.L., Fildani, A., Brunt, R.L, Hodgson, D.M. and Flint, S.S.** (2015)
964 U–Pb zircon tuff geochronology from the Karoo Basin, South Africa: implications of zircon
965 recycling on stratigraphic age controls. *International Geology Review*, **57**, 393–410.
- 966
- 967 **Moiola, R.J. and Weiser, D.** (1968) Textural parameters: An Evaluation. *Journal of Sedimentary*
968 *Petrology*, **38**, 45-53.
- 969
- 970 **Mohrig, D., and Buttles, J.,** 2007, Deep turbidity currents in shallow channels. *Geology*, v. 35, p.
971 155–158.
- 972
- 973 **Morris, W.R., Scheilhing, M.H., Wickens, DeV., Bouma, A.H.** (2000) Reservoir architecture of
974 deepwater sandstones: examples from the Skoorsteenber Formation, Tanqua Karoo Sub-Basin,
975 South Africa. In: P. Weimer, R.M. Slatt, A.H. Bouma, and D.T. Lawrence, eds., Deep-water
976 reservoirs of the world: Gulf Coast Section SEPM Foundation, Twentieth Annual Research
977 Conference, p. 1010-1032.
- 978
- 979 **Mutti, E. and Sonnino, M.** (1981) Compensational cycles: a diagnostic feature of turbidite
980 sandstone lobes. International Association of Sedimentologists 2nd European Meeting, Bologna,
981 Italy, 120-123.
- 982
- 983 **Parker, G., M. García, Y. Fukushima, and W. Yu** (1987), Experiments on turbidity currents over
984 an erodible bed. *Journal of Hydraulic Research*, **25**, 123–147.

985
986 **Piper, D.J.W., and Normark, W.R.** (1983) Turbidite depositional patterns and flow characteristics,
987 Navy submarine fan, California Borderland. *Sedimentology*, **30**, 681–694.
988
989 **Pirrie, D., Butcher, A.R., Power, M.R., Gottlieb, P., Miller, G.L.** (2004), “Rapid quantitative
990 mineral and phase analysis using automated scanning electron microscopy (QEMSCAN®); potential
991 applications in forensic geoscience”. In: Pye, K., Croft, D.J. (Eds.), *Forensic Geoscience, Principles,*
992 *Techniques and Applications*, Vol. 232. Geological Society Special Publication, London, pp 23–136.
993
994 **Pope, S.B.** (2000) *Turbulent Flows*. Cambridge University Press, Cambridge, UK, 771 pp.
995
996 **Porten, K.W., Kane, I.A., Warchol, M.J. and Southern, S.J.,** in press. A sedimentological
997 process-based approach to depositional reservoir quality of deep-marine sandstones: an example
998 from the Springar Formation, north-western Vøring Basin, Norwegian Sea. *Journal of Sedimentary*
999 *Research*.
1000
1001 **Poyatos-More, M., Jones, G. D., Brunt, R., David M. Hodgson, Richard J. Wild, & Flint,**
1002 **S.** (2016). Mud-dominated basin margin progradation: processes and implications. *Journal of*
1003 *Sedimentary Research*, **86**, 863-878.
1004
1005 **Prélat, A. and Hodgson, D.M.** (2013) *The full range of turbidite bed thickness patterns in*
1006 *submarine lobes: controls and implications*. *Journal of the Geological Society*, **170**, 209-214.
1007
1008 **Prélat, A., Hodgson, D.M. and Flint, S.S.** (2009) Evolution, architecture and hierarchy of
1009 distributary deep-water deposits: a high-resolution outcrop investigation from the Permian Karoo
1010 Basin, South Africa. *Sedimentology*, **56**, 2132-U25.
1011
1012 **Pyles, D.R. and Jennette, D.C.** (2009) Geometry and architectural associations of co-genetic
1013 debrite–turbidite beds in basin-margin strata, Carboniferous Ross Sandstone (Ireland): Applications
1014 to reservoirs located on the margins of structurally confined submarine fans. *Marine and Petroleum*
1015 *Geology*, **26**, 1974-1996.

1016

1017 **Pysklywec, R.N. and Mitrovica, J.X.** (1999) The role of subduction-induced subsidence in the
1018 evolution of the Karoo Basin. *The Journal of Geology*, **107**, 155-164.

1019

1020 **Sequeiros, O.E.** (2012) Estimating turbidity current conditions from channel morphology: A Froude
1021 number approach. *Journal of Geophysical Research*, **117**, C04003.

1022

1023 **Smith, R.H.M.** (1990) A review of stratigraphy and sedimentary environments of the Karoo basin of
1024 South Africa. *Journal of African Earth Sciences*, **10**, 117–137.

1025

1026 **Southern, S.J., Patacci, M., Felletti, F. and McCaffrey, W.D.** (2015) Influence of flow
1027 containment and substrate entrainment upon sandy hybrid event beds containing a co-genetic mud-
1028 clast-rich division. *Sedimentary Geology*, **321**. 105 - 122.

1029

1030 **Southern, S.J., Kane, I.A., Warchol, M.J., Porten, K.W. and McCaffrey, W.D.** (2016) Hybrid
1031 event beds dominated by transitional-flow facies: Character, distribution and significance in the
1032 Maastrichtian Springar Formation, north-west Vøring Basin, Norwegian Sea. *Sedimentology*,
1033 DOI: 10.1111/sed.12323

1034

1035 **Spychala, Y.T., Hodgson, D.M., Stevenson, C.J. and Flint, S.S.** (2016) Aggradational lobe fringes:
1036 The influence of subtle intrabasinal seabed topography on sediment gravity flow processes and lobe
1037 stacking patterns. *Sedimentology*. DOI: 10.1111/sed.12315

1038

1039 **Spychala, Y.T., Hodgson, D.M., Prelat, A., Kane, I.A., Flint, S.S. and Mountney, N.P.** (in press),
1040 Frontal and lateral submarine lobe fringes: Comparing sedimentary facies, architecture and flow
1041 processes. *Journal of Sedimentary Research*.

1042

1043 **Stevenson, C.J., Jackson, C.A.L., Hodgson, D.M., Hubbard, S.M., and Eggenhuisen, J.T.**
1044 (2015), Deep-water sediment bypass. *Journal of Sedimentary research*, **85**, 1058-1081.

1045

- 1046 **Sullivan, M.D., Jensen, G.N., Goulding, F.J., Jennette, D.C., Foreman, J.L. and Stern, D.**
1047 (2000) Architectural analysis of deep-water outcrops: Implications for exploration and production of
1048 the Diana Sub-basin, western Gulf of Mexico, *in* P. Weimer, R.M. Slatt, A.H. Bouma, and D.T.
1049 Lawrence, eds., Deep-water reservoirs of the world: Gulf Coast Section SEPM Foundation,
1050 Twentieth Annual Research Conference, p. 1010-1032.
- 1051
- 1052 **Sumner, E.J., Talling, P.J., and Amy, L.A.** (2009) Deposits of flows transitional between turbidity
1053 current and debris flow. *Geology*, **37**, 991–994, doi:10.1130/G30059A.1.
- 1054
- 1055 **Sylvester, Z. and Lowe, D.R.** (2004) Textural trends in turbidites and slurry beds from the
1056 Oligocene flysch of the East Carpathians, Romania. *Sedimentology*, **51**, 945-972.
- 1057
- 1058 **Talling, P.J., Amy, L.A., Wynn, R.B., Peakall, J. and Robinson, M.** (2004) Beds comprising
1059 debrite sandwiched within co-genetic turbidite: origin and widespread occurrence in distal
1060 depositional environments. *Sedimentology*, **51**, 163-194.
- 1061
- 1062 **Talling, P.J., Masson, D.G., Sumner, E.J. and Malgesini, G.** (2012) Subaqueous sediment density
1063 flows: Depositional processes and deposit types. *Sedimentology*, **59**, 1937-2003.
- 1064
- 1065 **Talling, P.J.** (2013) Hybrid submarine flows comprising turbidity current and cohesive debris flow:
1066 Deposits, theoretical and experimental analyses, and generalized models: *Geosphere*, 9, 1-28.
- 1067
- 1068 **Tankard A., Welsink H., Aukes P., Newton R., Stettler E.** (2009) Tectonic evolution of the Cape
1069 and Karoo basins of South Africa. *Marine and Petroleum Geology*, **26**, 1379–1412. doi:
1070 10.1016/j.marpetgeo.2009.01.022.
- 1071
- 1072
- 1073 **Terlaky, V., Arnott, R.W.C.** (2014) Matrix-rich and associated matrix-poor sandstones: avulsion
1074 splays in slope and basin-floor strata. *Sedimentology* **61**, 1175-1197.
1075 <http://dx.doi.org/10.1111/sed.12096>.
- 1076
- 1077 **Twichell, D., Nelson, C.H., Kenyon, N. and Schwab, W.** (2009) The Influence of External
1078 Processes on the Holocene Evolution of the Mississippi Fan, *in* B. Kneller, O.J. Martinsen, and B.

1079 McCaffrey, eds., External Controls on Deep-Water Depositional: SEPM Special Publication **92**,
1080 145-157.
1081
1082 **van der Werff, W. and Johnson, S.** (2003a) High resolution stratigraphic analysis of turbidite
1083 system, Tanqua Karoo Basin, South Africa. *Marine and Petroleum Geology*, **20**, 45-69.
1084
1085 **van der Werff, W. and Johnson, S.D.** (2003b) Deep-sea fan pinch-out geometries and their
1086 relationship to fan architecture, Tanqua Karoo basin (South Africa). *International Journal of Earth*
1087 *Sciences*, **92**, 728-742.
1088
1089 **Veevers, J.J., Cole, D.I. and Cowan, E.J.** (1994) Souther Africa: Karoo Basin and Cape Fold Belt.
1090 In: *Permian-Triassic Pangean Basins and Foldbelts Along the Panthalassan Margin of*
1091 *Gondwanaland* (Eds J.J. Veevers and C.M. Powek), **Memoir 184**, pp. 223-279. Geological Society
1092 of America.
1093
1094 **Visser, J.N.J.** (1997) Deglaciation sequences in the Permo-Carboniferous Karoo and Kalahari
1095 basins of the southern Africa: a toll in the analysis of cyclic glaciomarine basin fills. *Sedimentology*,
1096 **44**, 507-521.
1097
1098 **Visser, J.N.J. and Prackelt, H.E.** (1996) Subduction, mega-shear systems and Late Palaeozoic
1099 basin development in the African segment of Gondwana. *Geologische Rundschau*, **85**, 632-646.
1100
1101 **Wan, Z.** (1982) Bed Material Movement in Hyperconcentrated Flow. Institute of Hydrodynamics
1102 and Hydraulic Engineering, Technical University of Denmark, Lyngby, Series Paper, pp. 16-24.
1103
1104 **Wickens, H.J.** (1994) *Basin floor fan building turbidites of the southwestern Karoo Basin, Permian*
1105 *Ecca Group, South Africa*, University of Port Elizabeth, Unpublished, 233 pp.
1106
1107 **Wild, R., Hodgson, D. and Flint, S.** (2005) Architecture and stratigraphic evolution of multiple,
1108 vertically-stacked slope channel complexes, Tanqua depocentre, Karoo Basin, South Africa. In:
1109 *Submarine slope systems: processes and products* (Eds D. Hodgson and S. Flint), **244**, pp. 89-111.
1110 The Geological Society of London, London.
1111

1112 **Wild, R., Flint, S.S. and Hodgson, D.M.** (2009) Stratigraphic evolution of the upper slope and shelf
1113 edge in the Karoo Basin, South Africa. *Basin Research*, **21**, 502-527.

1114
1115 **Wintwerp, J.C., and van Kesteren, W.G.M.** (2004). Introduction to the Physics of Cohesive
1116 Sediment in the Marine Environment: Oxford, U.K., Elsevier, Developments in Sedimentology 56,
1117 559 p.

1118
1119 **Wood, A. and Smith, A., J.,** (1958) The Sedimentation and Sedimentary History of the
1120 Aberystwyth Grits (Upper Llandoveryan). *Quarterly Journal of the Geological Society*, **114**, 163-
1121 195.

1122
1123 **Zarra, L.,** (2007) Chronostratigraphic Framework for the Wilcox Formation (Upper Paleocene-
1124 Lower Eocene) in the Deep-Water Gulf of Mexico: Biostratigraphy, Sequences, and Depositional
1125 Systems. In: Kennan, L., Pindell, J., and Rosen, N.C., eds., The Paleogene of the Gulf of Mexico and
1126 Caribbean Basins: Processes, Events, and Petroleum Systems: GCSSEPM Foundation 27th Annual
1127 Bob F. Perkins Research Conference, p. 81–145.

1128 **Zhiyao, S., Tingting, W., Fumin, X. and Ruijie, L.** (2008). A simple formula for predicting
1129 settling velocity of sediment particles. *Water Science and Engineering Journal*, **1**, 37– 43.

1130

1131

1132

1133

1134

1135

1136

1137

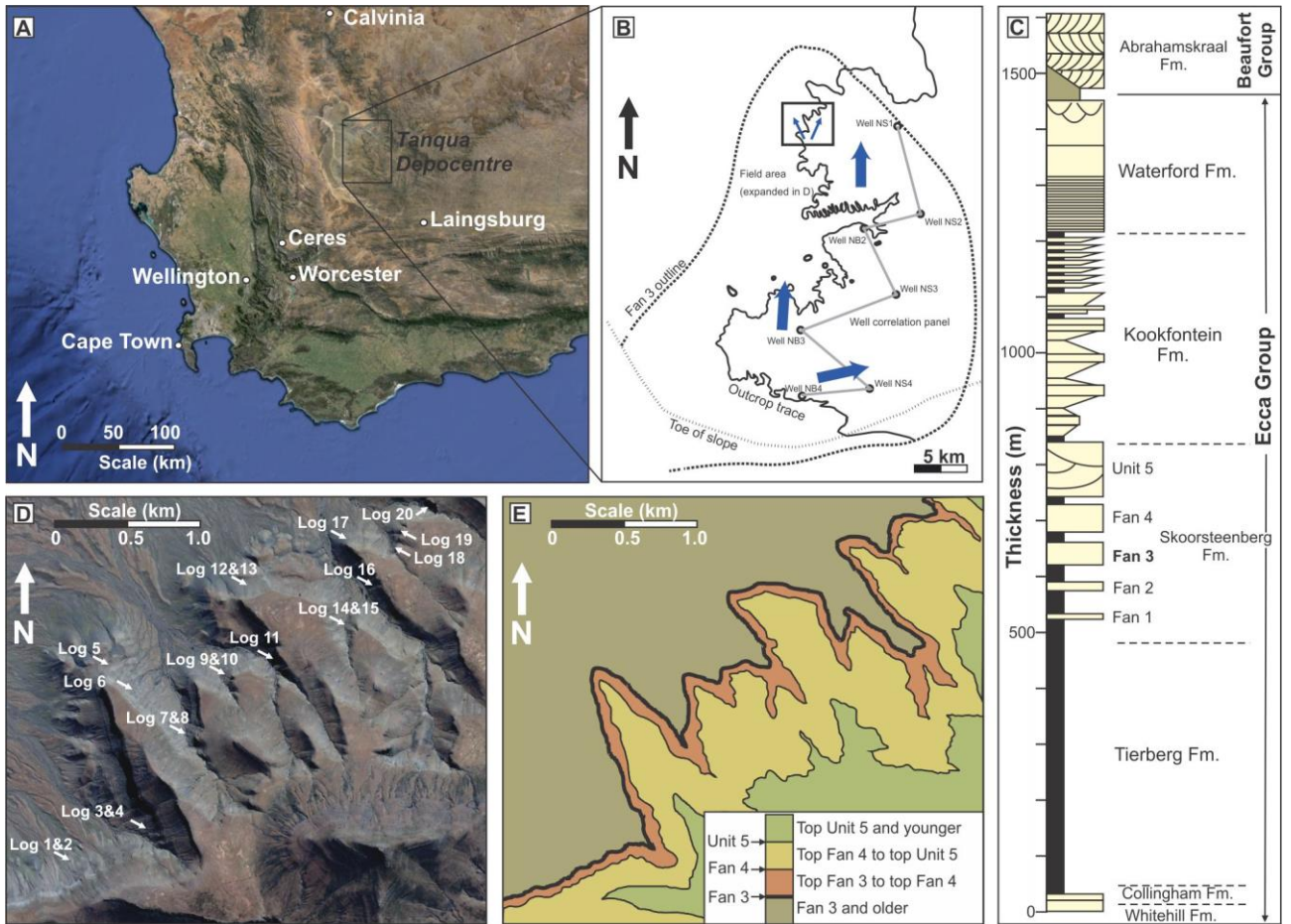
1138 **Table & Figure Captions**

Id	SK2A				SK3A				SK3D				SK4A				SK4E				SK4G				SK4H				SK4I			
	SK2A	SK2B	SK2C	SK2D	SK3A	SK3B	SK3C	SK3D	SK3E	SK3F	SK3G	SK3H	SK4A	SK4B	SK4C	SK4D	SK4E	SK4F	SK4G	SK4H	SK4I	SK4J	SK4K	SK4L	SK4M	SK4N	SK4O	SK4P	SK4Q	SK4R	SK4S	SK4T
Bed Type	HB-base	HB	HB	HB-top	TURB-base	TURB	TURB-top	AMAL-base	AMAL	AMAL-top	AMAL-mid	HB-base	HB	HB	HB-top	HB-base	HB	HB	HB-top	HB-base	HB	HB	HB-top	HB-base	HB	HB	HB-top	HB-base	HB	HB	HB-top	
Mineral Mass (%)	46.25	44.95	41.84	31.86	46.07	47.38	38.78	44.48	42.99	42.77	42.77	38.08	32.08	37.00	30.67	41.96	34.79	37.51	36.27	30.87	31.88	24.83	28.37	30.81	29.63	25.16	25.16	25.16	25.16	25.16	25.16	
Quartz	34.87	35.53	33.42	28.82	35.49	35.47	33.12	33.32	34.80	34.74	34.74	32.73	28.36	31.88	24.83	32.38	28.37	30.81	29.63	25.16	25.16	25.16	25.16	25.16	25.16	25.16	25.16	25.16	25.16	25.16	25.16	
Plagioclase	2.00	1.89	1.97	2.01	1.91	1.81	1.80	2.05	1.72	2.16	2.16	2.40	2.11	2.54	1.30	2.37	1.80	1.80	1.94	1.34	1.34	1.34	1.34	1.34	1.34	1.34	1.34	1.34	1.34	1.34	1.34	
K-Feldspar	1.01	0.96	0.98	1.82	0.90	1.00	1.45	1.02	1.03	1.02	1.02	1.35	1.87	1.35	1.73	1.18	1.52	1.52	1.58	1.63	1.63	1.63	1.63	1.63	1.63	1.63	1.63	1.63	1.63	1.63	1.63	
Muscovite	9.02	9.78	12.81	22.28	8.67	8.30	15.31	9.42	8.83	9.84	9.84	15.79	25.69	17.36	32.89	12.93	24.55	18.24	19.52	31.98	31.98	31.98	31.98	31.98	31.98	31.98	31.98	31.98	31.98	31.98	31.98	
Illite	3.78	3.25	5.15	8.03	3.71	3.41	6.05	6.68	6.26	4.46	4.46	5.31	5.21	5.92	4.40	4.74	4.64	5.94	6.44	5.22	5.22	5.22	5.22	5.22	5.22	5.22	5.22	5.22	5.22	5.22	5.22	
Chlorite	0.81	1.34	1.27	1.84	1.11	0.81	1.40	1.10	0.87	0.76	0.76	2.07	1.69	1.58	1.50	1.86	1.75	1.61	1.73	1.99	1.99	1.99	1.99	1.99	1.99	1.99	1.99	1.99	1.99	1.99	1.99	
Other clays	0.11	0.10	0.29	0.13	0.00	0.00	0.00	0.00	0.16	0.26	0.26	0.00	0.00	0.00	0.00	0.00	0.00	0.00	0.00	0.00	0.00	0.00	0.00	0.00	0.00	0.00	0.00	0.00	0.00	0.00	0.00	
Calcite	0.99	0.88	0.95	1.71	0.82	0.75	0.91	0.76	0.76	0.82	0.82	0.98	1.51	0.96	1.06	0.92	1.17	1.15	1.20	0.88	0.88	0.88	0.88	0.88	0.88	0.88	0.88	0.88	0.88	0.88	0.88	
Rutile	0.39	0.33	0.37	0.58	0.44	0.42	0.51	0.40	0.35	0.33	0.33	0.45	0.55	0.47	0.67	0.46	0.53	0.55	0.55	0.62	0.62	0.62	0.62	0.62	0.62	0.62	0.62	0.62	0.62	0.62	0.62	
Apatite	0.05	0.02	0.02	0.02	0.06	0.04	0.03	0.07	0.07	0.02	0.02	0.02	0.03	0.02	0.02	0.03	0.02	0.02	0.03	0.01	0.01	0.01	0.01	0.01	0.01	0.01	0.01	0.01	0.01	0.01	0.01	
Zircon	0.01	0.04	0.02	0.02	0.27	0.03	0.03	0.02	0.02	0.01	0.01	0.02	0.02	0.04	0.05	0.06	0.02	0.01	0.01	0.02	0.02	0.02	0.02	0.02	0.02	0.02	0.02	0.02	0.02	0.02	0.02	
Others	0.71	0.94	0.90	0.89	0.57	0.56	0.63	0.68	0.54	0.67	0.67	0.81	0.89	0.88	0.90	1.12	0.84	0.83	0.80	0.96	0.96	0.96	0.96	0.96	0.96	0.96	0.96	0.96	0.96	0.96	0.96	
Unclassified	46.71	45.42	42.35	32.56	46.56	47.79	39.33	44.93	43.42	43.21	43.21	38.66	32.78	37.56	31.39	42.52	35.48	38.14	36.92	30.87	31.88	24.83	28.37	30.81	29.63	25.16	25.16	25.16	25.16	25.16	25.16	
Mineral Volume (%)	35.28	35.97	33.90	29.51	35.93	35.84	33.65	33.72	35.21	35.16	35.16	33.30	29.03	32.42	25.46	32.88	28.99	31.39	30.53	25.77	25.77	25.77	25.77	25.77	25.77	25.77	25.77	25.77	25.77	25.77	25.77	
Quartz	2.07	1.96	2.04	2.11	1.98	1.88	1.87	2.12	1.79	2.24	2.24	2.50	2.21	2.64	1.36	2.46	1.89	1.87	2.02	1.41	1.41	1.41	1.41	1.41	1.41	1.41	1.41	1.41	1.41	1.41	1.41	
Plagioclase	0.95	0.90	0.92	1.73	0.84	0.94	1.37	0.96	0.97	0.96	0.96	1.28	1.77	1.28	1.64	1.11	1.44	1.44	1.49	1.55	1.55	1.55	1.55	1.55	1.55	1.55	1.55	1.55	1.55	1.55	1.55	
K-Feldspar	8.70	9.43	12.38	21.73	8.36	7.99	14.82	9.08	8.51	9.49	9.49	15.30	25.06	16.83	32.14	12.51	23.90	17.70	18.97	31.22	31.22	31.22	31.22	31.22	31.22	31.22	31.22	31.22	31.22	31.22	31.22	
Muscovite	3.78	3.25	5.17	8.12	3.71	3.41	6.07	6.68	6.26	4.46	4.46	5.34	5.28	5.95	4.46	4.76	4.69	5.99	6.49	5.29	5.29	5.29	5.29	5.29	5.29	5.29	5.29	5.29	5.29	5.29	5.29	
Illite	0.73	1.18	1.13	1.64	0.98	0.73	1.24	0.97	0.77	0.67	0.67	1.82	1.53	1.41	1.38	1.65	1.58	1.43	1.54	1.82	1.82	1.82	1.82	1.82	1.82	1.82	1.82	1.82	1.82	1.82	1.82	
Chlorite	0.11	0.10	0.28	0.13	0.00	0.00	0.00	0.00	1.72	2.33	2.33	0.00	0.00	0.00	0.00	0.00	0.00	0.00	0.00	0.00	0.00	0.00	0.00	0.00	0.00	0.00	0.00	0.00	0.00	0.00	0.00	
Other clays	0.62	0.55	0.59	1.08	0.51	0.47	0.57	0.47	0.47	0.51	0.51	0.62	0.95	0.60	0.67	0.58	0.73	0.72	0.76	0.56	0.56	0.56	0.56	0.56	0.56	0.56	0.56	0.56	0.56	0.56	0.56	
Calcite	0.32	0.27	0.31	0.46	0.37	0.35	0.42	0.34	0.29	0.27	0.27	0.37	0.46	0.40	0.56	0.38	0.44	0.46	0.46	0.52	0.52	0.52	0.52	0.52	0.52	0.52	0.52	0.52	0.52	0.52	0.52	
Rutile	0.03	0.01	0.01	0.01	0.03	0.03	0.02	0.04	0.04	0.01	0.01	0.01	0.01	0.01	0.01	0.02	0.01	0.01	0.02	0.01	0.01	0.01	0.01	0.01	0.01	0.01	0.01	0.01	0.01	0.01	0.01	
Apatite	0.01	0.03	0.02	0.02	0.16	0.02	0.02	0.02	0.02	0.01	0.01	0.01	0.02	0.03	0.04	0.04	0.01	0.01	0.01	0.02	0.02	0.02	0.02	0.02	0.02	0.02	0.02	0.02	0.02	0.02	0.02	
Others	0.70	0.93	0.89	0.88	0.56	0.55	0.62	0.67	0.53	0.66	0.66	0.80	0.88	0.87	0.89	1.10	0.83	0.82	0.79	0.95	0.95	0.95	0.95	0.95	0.95	0.95	0.95	0.95	0.95	0.95	0.95	
Unclassified	39.24	36.53	36.74	35.97	42.00	37.23	36.61	43.92	35.12	35.12	35.12	44.93	36.45	37.56	31.39	48.58	38.92	32.19	31.60	30.49	31.60	24.83	28.37	30.81	29.63	25.16	25.16	25.16	25.16	25.16	25.16	
Mineral Volume (%)	29.23	27.28	29.11	26.11	32.18	30.57	29.40	29.25	24.56	24.56	24.56	31.18	27.06	29.12	23.65	26.27	26.87	27.02	27.02	25.77	25.77	25.77	25.77	25.77	25.77	25.77	25.77	25.77	25.77	25.77	25.77	
Quartz	2.63	2.53	2.05	1.83	2.04	2.09	2.09	1.93	1.66	1.66	1.66	2.16	1.96	1.96	1.86	2.31	2.24	1.83	2.07	1.68	1.68	1.68	1.68	1.68	1.68	1.68	1.68	1.68	1.68	1.68	1.68	
Plagioclase	1.42	1.81	2.27	1.68	1.26	1.59	1.89	1.18	1.57	1.57	1.57	1.09	1.84	1.76	1.09	1.69	1.99	2.11	1.27	1.08	1.08	1.08	1.08	1.08	1.08	1.08	1.08	1.08	1.08	1.08	1.08	
K-Feldspar	19.02	21.80	19.49	23.33	13.58	18.89	19.41	14.51	27.90	12.02	12.02	6.64	12.82	27.85	19.52	6.64	27.37	26.05	7.81	24.46	24.46	24.46	24.46	24.46	24.46	24.46	24.46	24.46	24.46	24.46	24.46	
Muscovite	5.16	5.13	5.98	6.25	5.41	5.41	5.27	5.66	5.41	5.22	5.22	5.73	5.70	4.36	7.25	4.82	5.72	7.49	4.92	7.41	7.41	7.41	7.41	7.41	7.41	7.41	7.41	7.41	7.41	7.41	7.41	
Illite	1.63	1.96	1.77	1.88	1.26	1.88	2.26	1.43	1.68	1.65	1.65	2.31	2.01	1.19	1.75	1.58	1.82	2.27	1.32	1.91	1.91	1.91	1.91	1.91	1.91	1.91	1.91	1.91	1.91	1.91	1.91	
Chlorite	0.00	0.45	0.22	0.00	0.00	0.00	0.00	0.00	0.00	0.00	0.00	0.00	0.00	0.00	0.00	0.00	0.00	0.00	0.00	0.00	0.00	0.00	0.00	0.00	0.00	0.00	0.00	0.00	0.00	0.00	0.00	
Other clays	0.50	0.54	0.54	0.60	0.55	0.52	0.51	0.47	0.61	0.41	0.41	0.55	0.50	0.39	0.42	0.54	0.58	0.61	0.37	0.63	0.63	0.63	0.63	0.63	0.63	0.63	0.63	0.63	0.63	0.63	0.63	
Calcite	0.39	0.37	0.43	0.46	0.42	0.38	0.38	0.42	0.45	0.39	0.39	0.39	0.39	0.28	0.34	0.42	0.42	0.46	0.32	0.47	0.47	0.47	0.47	0.47	0.47	0.47	0.47	0.47	0.47	0.47	0.47	
Rutile	0.01	0.01	0.01	0.01	0.02	0.01	0.01	0.01	0.01	0.01	0.01	0.01	0.01	0.01	0.01	0.01	0.01	0.01	0.02	0.01	0.01	0.01	0.01	0.01	0.01	0.01	0.01	0.01	0.01	0.01	0.01	
Apatite	0.09	0.15	0.05	0.09	0.03	0.25	0.30	0.06	0.04	0.05	0.04	0.04	0.04	0.17	0.11	0.03	0.11	0.20	0.03	0.22	0.22	0.22	0.22	0.22	0.22	0.22	0.22	0.22	0.22	0.22	0.	

Sample name	Bed Type	Grain count	Vectorial mean (M)	Mean vector magnitude (R)	Vectorial concentration (K)	Distribution type (0.05)
2A	TFD	55243	27.10	0.11	0.23	Von Mises
2B	TFD	59868	19.71	0.18	0.36	Von Mises
2C	TFD	59245	1.32	0.09	0.17	Von Mises
2D	TFD	101249	14.04	0.25	0.52	Von Mises
3A	Turbidite	73993	159.35	0.10	0.21	Von Mises
3B	Turbidite	61991	136.56	0.02	0.04	Uniform
3C	Turbidite	146406	9.15	0.29	0.60	Von Mises
3D	Amal. Turbidite	48116	5.69	0.12	0.24	Von Mises
3E	Amal. Turbidite	44879	20.18	0.17	0.34	Von Mises
3F	Amal. Turbidite	56065	26.47	0.07	0.13	Uniform
4A	TFD	33527	22.88	0.16	0.32	Von Mises
4B	TFD	88577	176.47	0.19	0.39	Von Mises
4C	TFD	80043	1.78	0.19	0.39	Von Mises
4D	TFD	35400	8.86	0.34	0.72	Von Mises
4E	TFD	67770	161.69	0.17	0.34	Von Mises
4F	TFD	71208	10.71	0.22	0.45	Von Mises
4G	TFD	113744	175.94	0.22	0.46	Von Mises
4H	TFD	98892	9.45	0.28	0.57	Von Mises
4I	TFD	37427	178.45	0.33	0.69	Von Mises
12A	TFD	43312	1.19	0.25	0.51	Von Mises
12B	TFD	46508	13.38	0.31	0.65	Von Mises
12C	TFD	40441	167.34	0.17	0.35	Von Mises
12D	TFD	8246	7.18	0.35	0.75	Von Mises
12E	TFD	74736	21.73	0.28	0.59	Von Mises
12F	TFD	38182	6.53	0.22	0.45	Von Mises
12G	TFD	56020	176.10	0.12	0.25	Von Mises
13A	TFD	53342	2.39	0.26	0.53	Von Mises
13B	TFD	5934	8.84	0.32	0.68	Von Mises
13C	TFD	32897	10.16	0.23	0.48	Von Mises
13D	TFD	27875	158.87	0.24	0.50	Von Mises
13E	TFD	45056	176.67	0.24	0.48	Von Mises
13F	Turbidite	32994	162.82	0.14	0.27	Von Mises
13G	Turbidite	70501	151.62	0.05	0.10	Uniform
13H	TFD	9710	12.33	0.22	0.45	Von Mises
13I	TFD	28323	176.61	0.27	0.56	Von Mises
13J	TFD	6768	5.96	0.33	0.71	Von Mises
13K	TFD	13707	2.09	0.13	0.27	Uniform
13L	TFD	22479	5.79	0.25	0.53	Von Mises
14A	Amal. Turbidite	59829	175.50	0.19	0.38	Von Mises

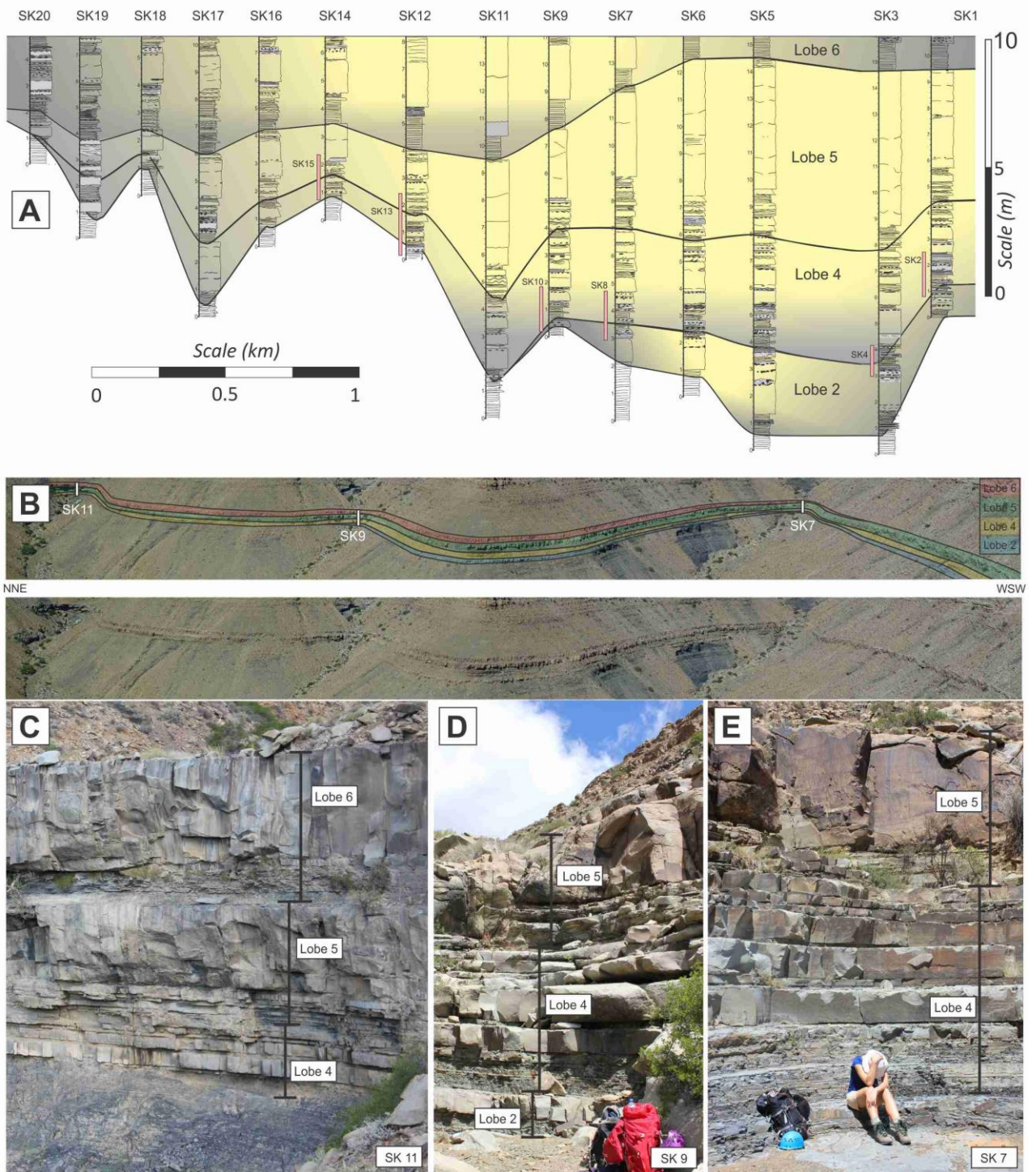
1143

1144 Table 2. Grain fabric data. Heavy outlines mark individual beds, which are classified here as HB (hybrid bed), TURB (turbidite) and AMAL (thick
1145 amalgamated sandstone – see text).



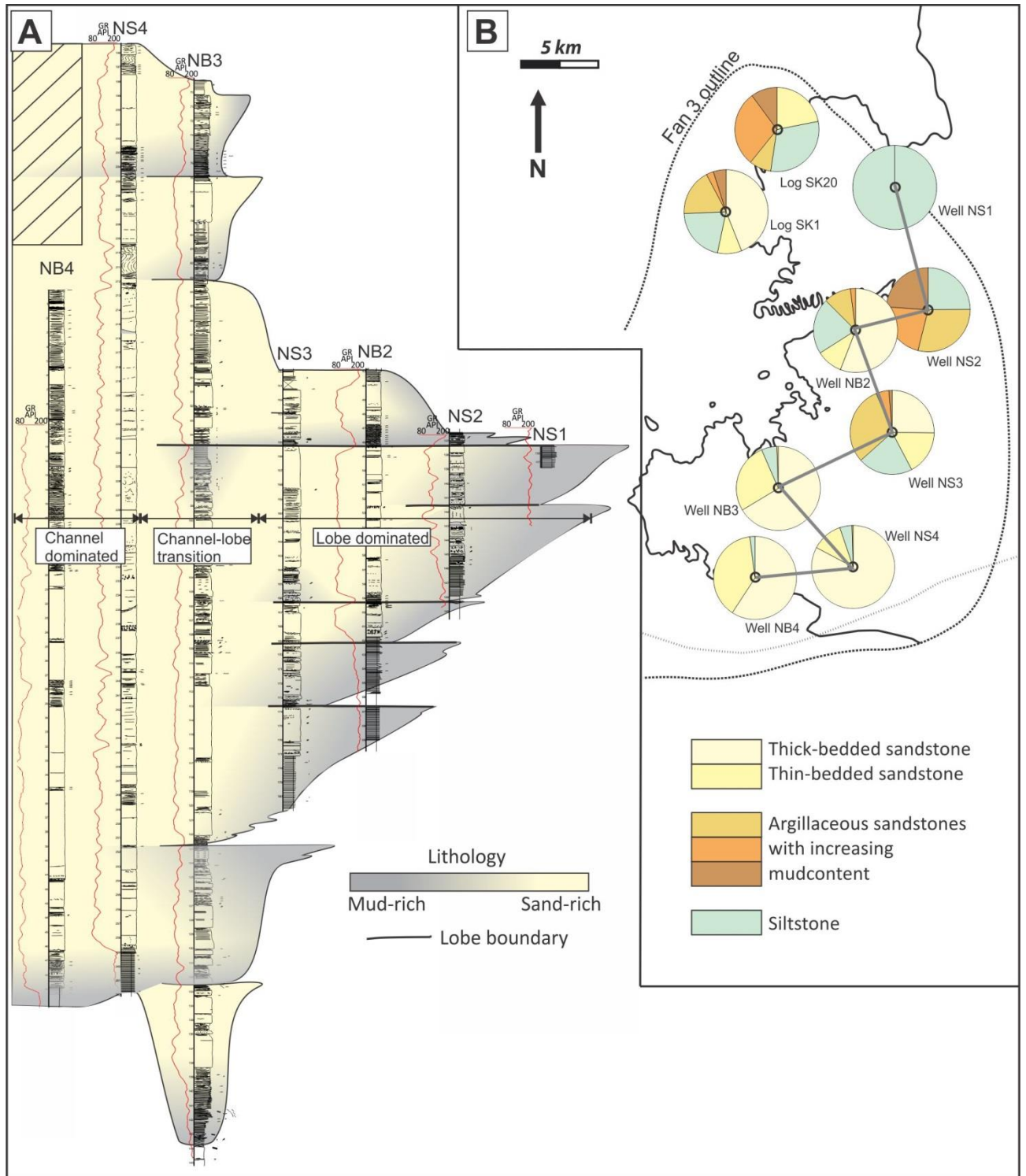
1146

1147 Figure 1. A) Aerial image of part of South Africa, highlighting the location of the Tanqua Depocentre, approximately 90 km northwest of the town of
 1148 Laingsburg. B) Outline of Fan 3 in the Tanqua Depocentre (from Hodgson et al., 2006); the field area is boxed and expanded in 'D' and 'E'. Blue
 1149 arrows show the general palaeoflow trends. C) Aerial image of the field area, illustrating the outcrop continuity of the near horizontal bedding surfaces,
 1150 and the location of the measured sections. D) Schematic stratigraphic log of the Permian to earliest Triassic deep-marine to fluvial fill of the Tanqua
 1151 depocentre (modified from Wild et al., 2005). E) Simple geological map illustrating the position of Fan 3 (bold line) and stratigraphic packages
 1152 between fan tops. At this scale the fan tops are the only mappable surfaces, as the fans tend to weather into steep outcrop faces, whereas the finer-
 1153 grained inter-fans form gentler slopes. The sandy part of Fan 2 has pinched out in this area (pinching out to the north), and is beneath the resolution of
 1154 this map; Fan 1 has pinched out. The uppermost package, i.e., 'Top Unit 5 and younger', is predominantly the Kookfontein Fm.



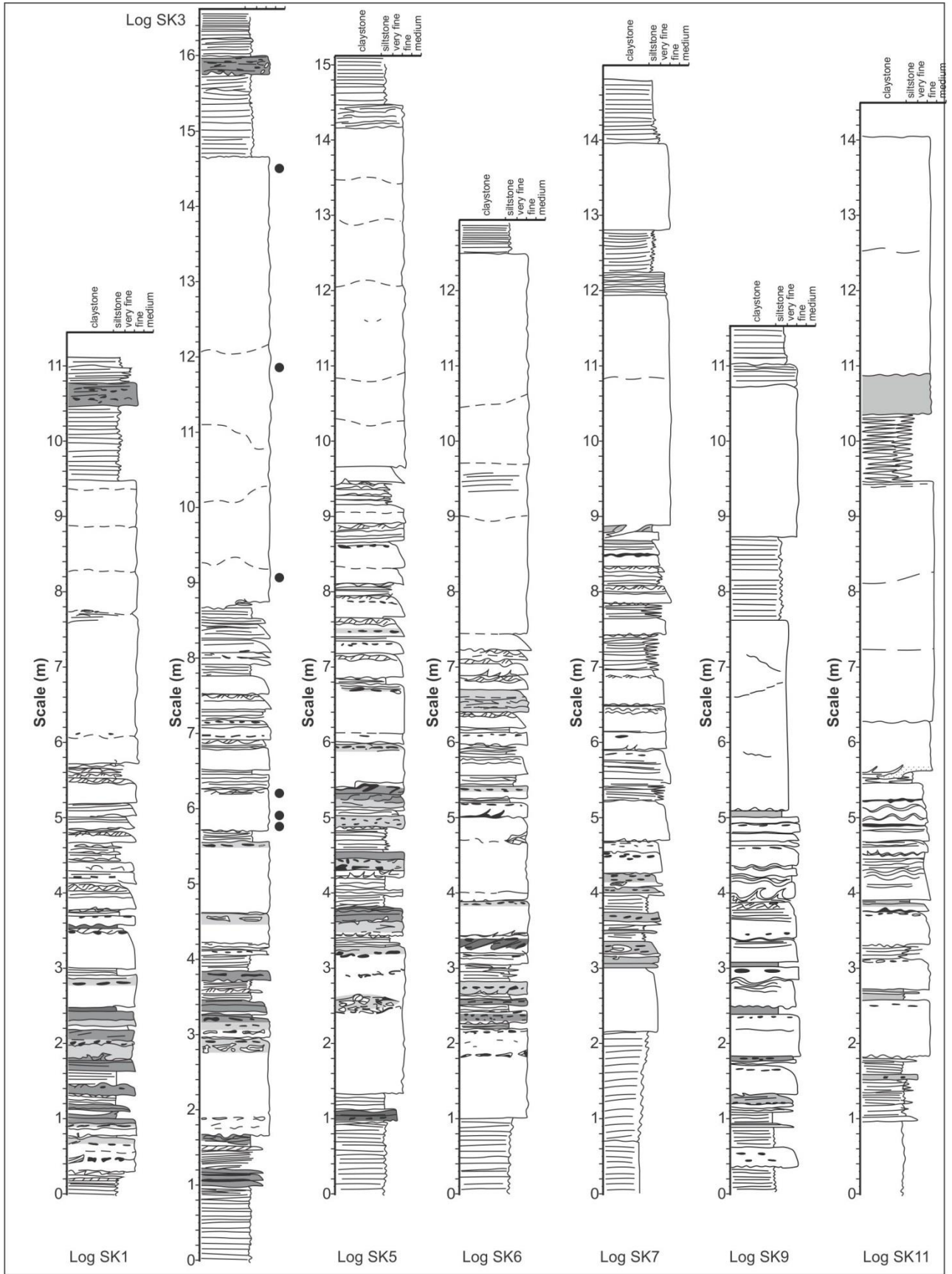
1155

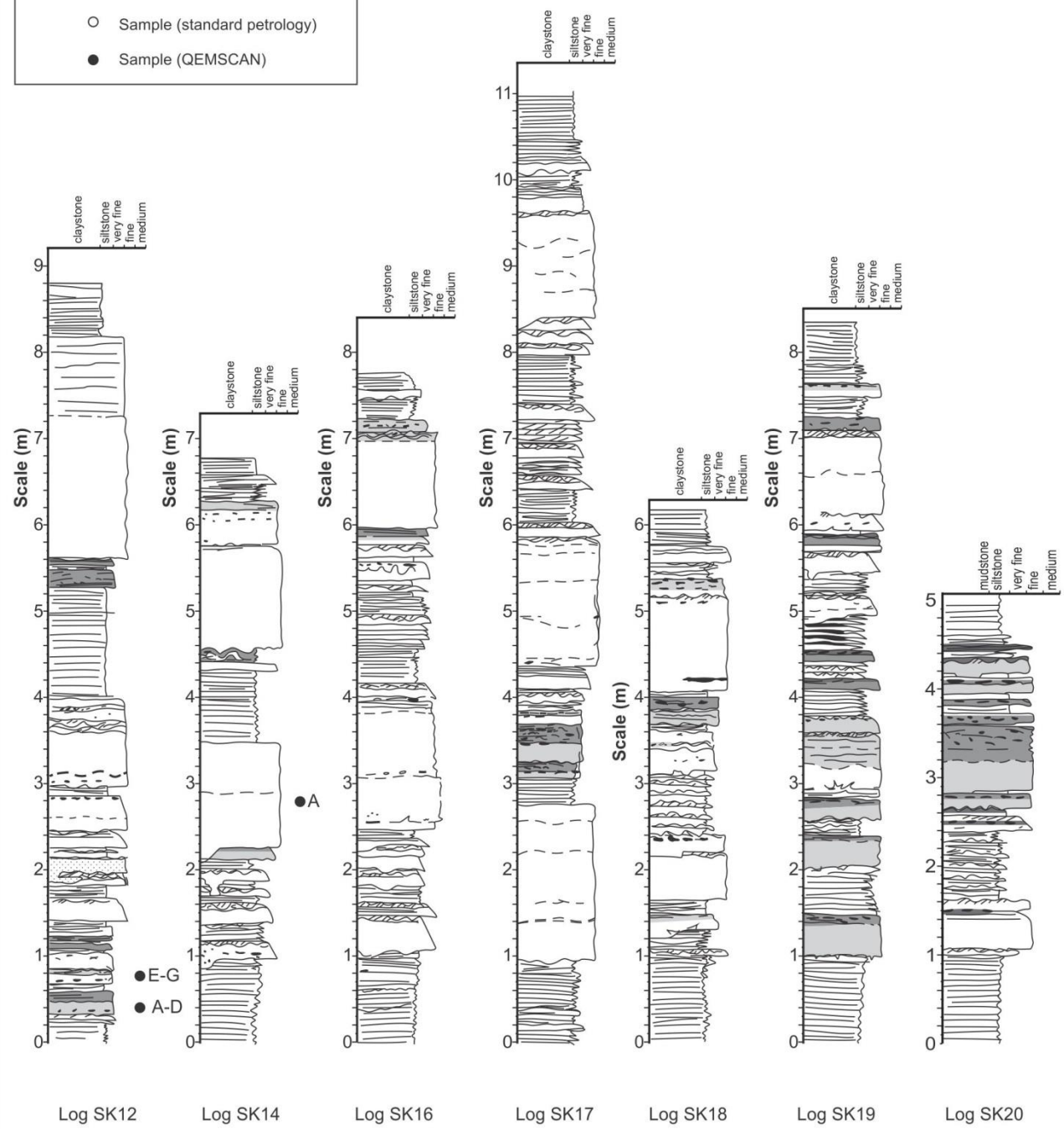
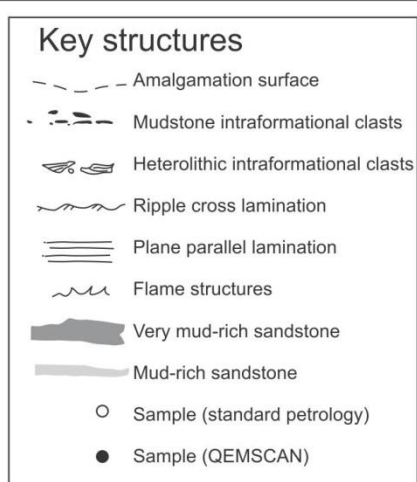
1156 Figure 2. A) Correlation panel of 1:20 outcrop logs SK1-20; positions of 1:2 logs are shown alongside the relevant log. The correlations are based on
 1157 walking out key stratigraphic surfaces, the lobes stack to form a lobe complex (Fan 3). Note that lobes 1 and 3 have pinched out in this position. The
 1158 outcrop panel (B) shows the general character and exposure of the distal parts of Fan 3. C, D and E illustrate the general outcrop character at the
 1159 positions of logs SK11, SK9 and SK7 respectively. The yellow and grey colouring gives a general indication of the sandstone (yellow) and mudstone
 1160 (grey) distribution. Palaeoflow is to the north, approximately right to left in the image.



1161

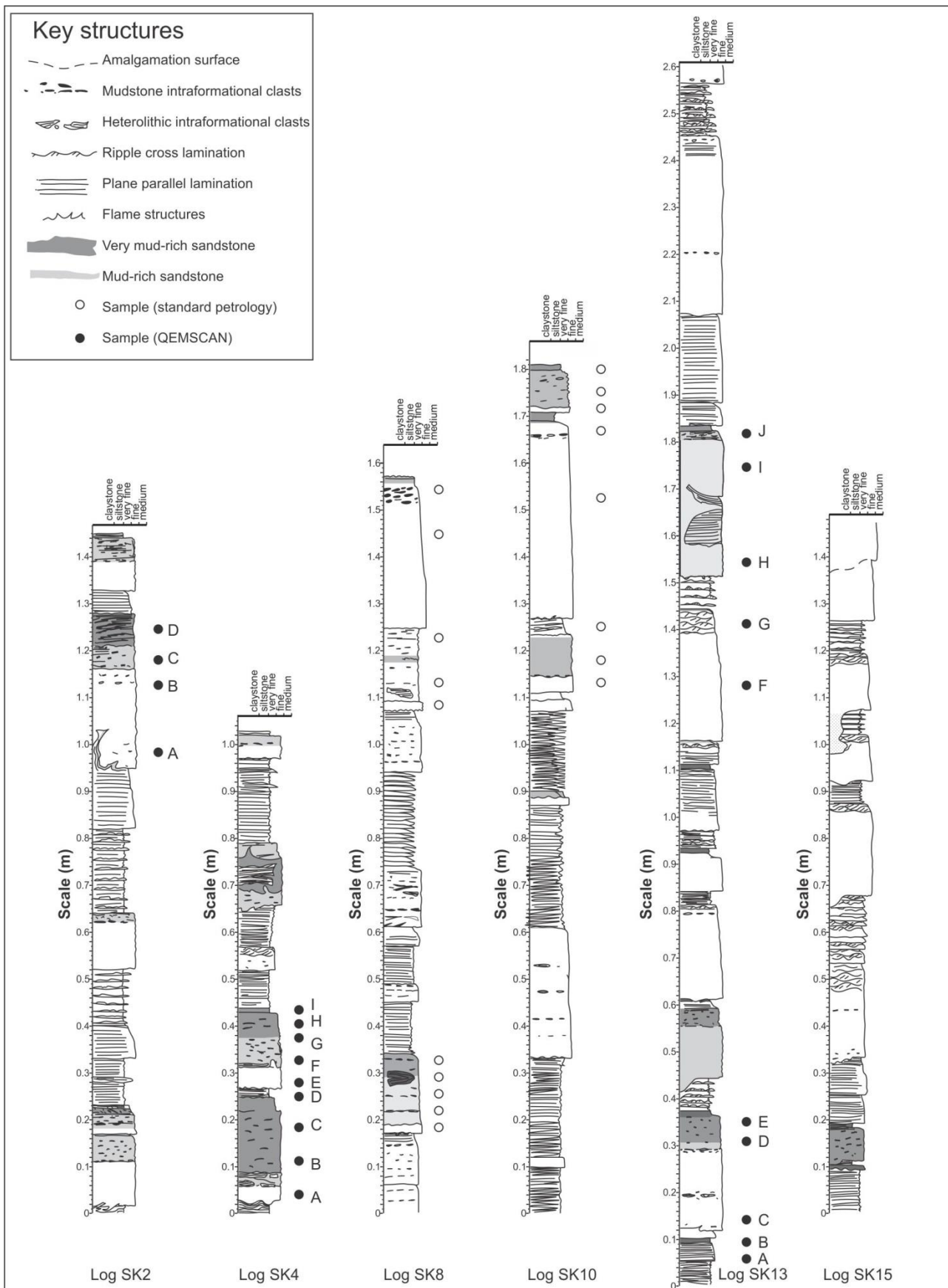
1162 Figure 3. (A) Correlation panel of logged sections from behind outcrop boreholes, spanning Fan 3 from the proximal channel-dominated part
 1163 (Ongeluk River outcrops), to the channel-lobe transition and across the lobe to the distal parts studied here (e.g., Boreholes NB2-NS1). Note that the
 1164 environments indicated are at the point of the arrows, not spanning the entire fan at that location. Correlations are tentative owing to the complex
 1165 nature of compensational lobe stacking patterns and based on finer-grained intervals subdividing the sandstone rich element, following Prélat et al.,
 1166 2009. A clear facies trend is observed across the lobe complex, illustrated by the plan view image (B).





1168

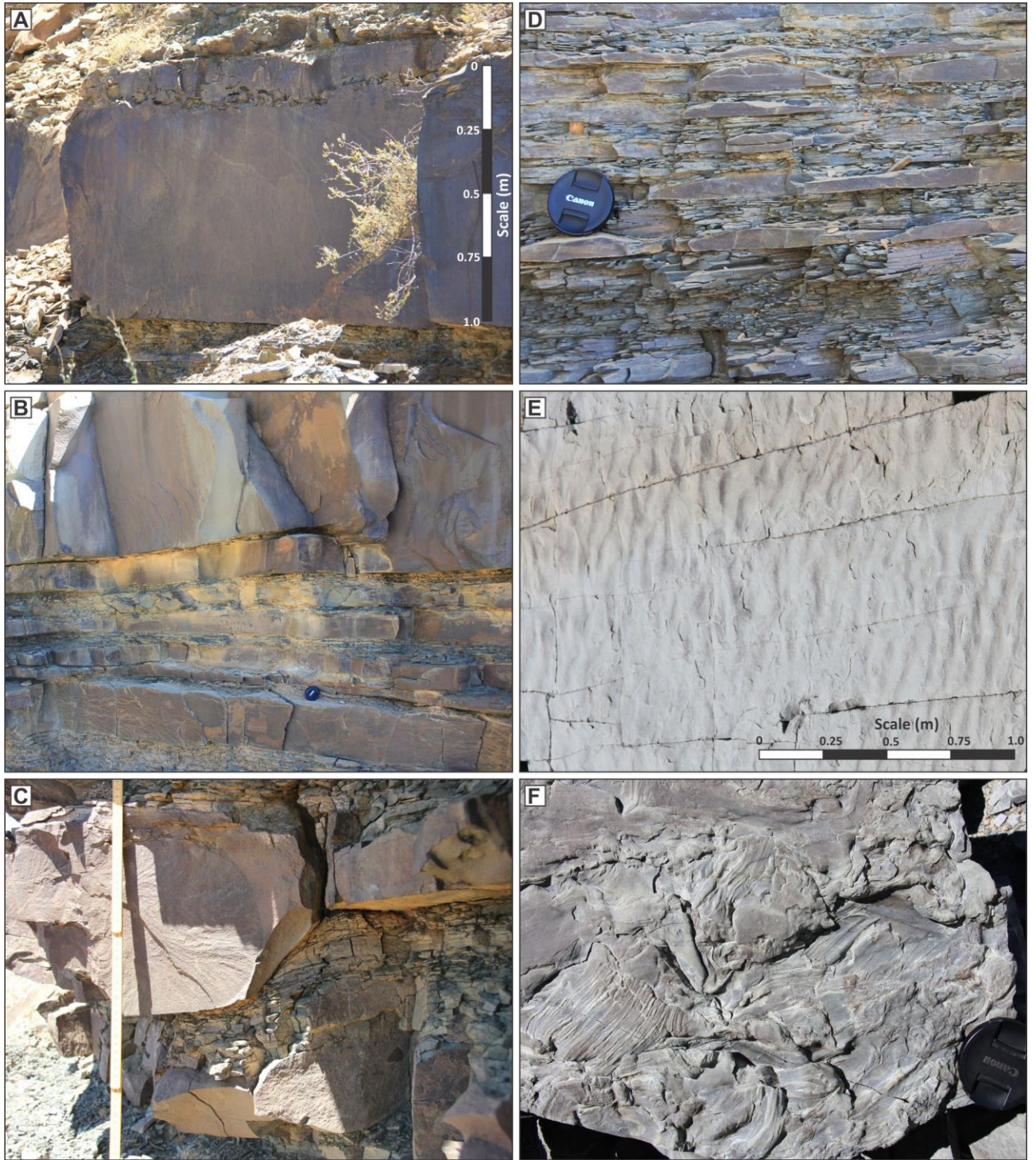
1169 Figure 4. Sedimentary logs through Fan 3, positions shown in Figure 1.



1170

1171

Figure 5. Detailed sedimentary logs from Fan 3, positions shown in Figure 1.



1172

1173
 1174
 1175
 1176
 1177

Fig. 6. Representative turbidite facies. A) Thick bedded turbidite with a sharp base, weak normal grading and with a clast-rich upper part; clasts are partly disaggregated generating clay-rich patches within the sandstone. B) Erosional bed bases typically plane out on mudstones and cut downwards in a stepwise manner through thin-bedded intervals, occasionally with contemporaneous lateral injection. C) Erosional step at base of medium-bedded sandstone which is loaded into underlying thin-bedded silty turbidites. D) Thin-bedded very-fine-grained low-density turbidites. E) Rippled bed top to low density turbidite. F) Plant imprints in an intra-bed division.



1178

1179

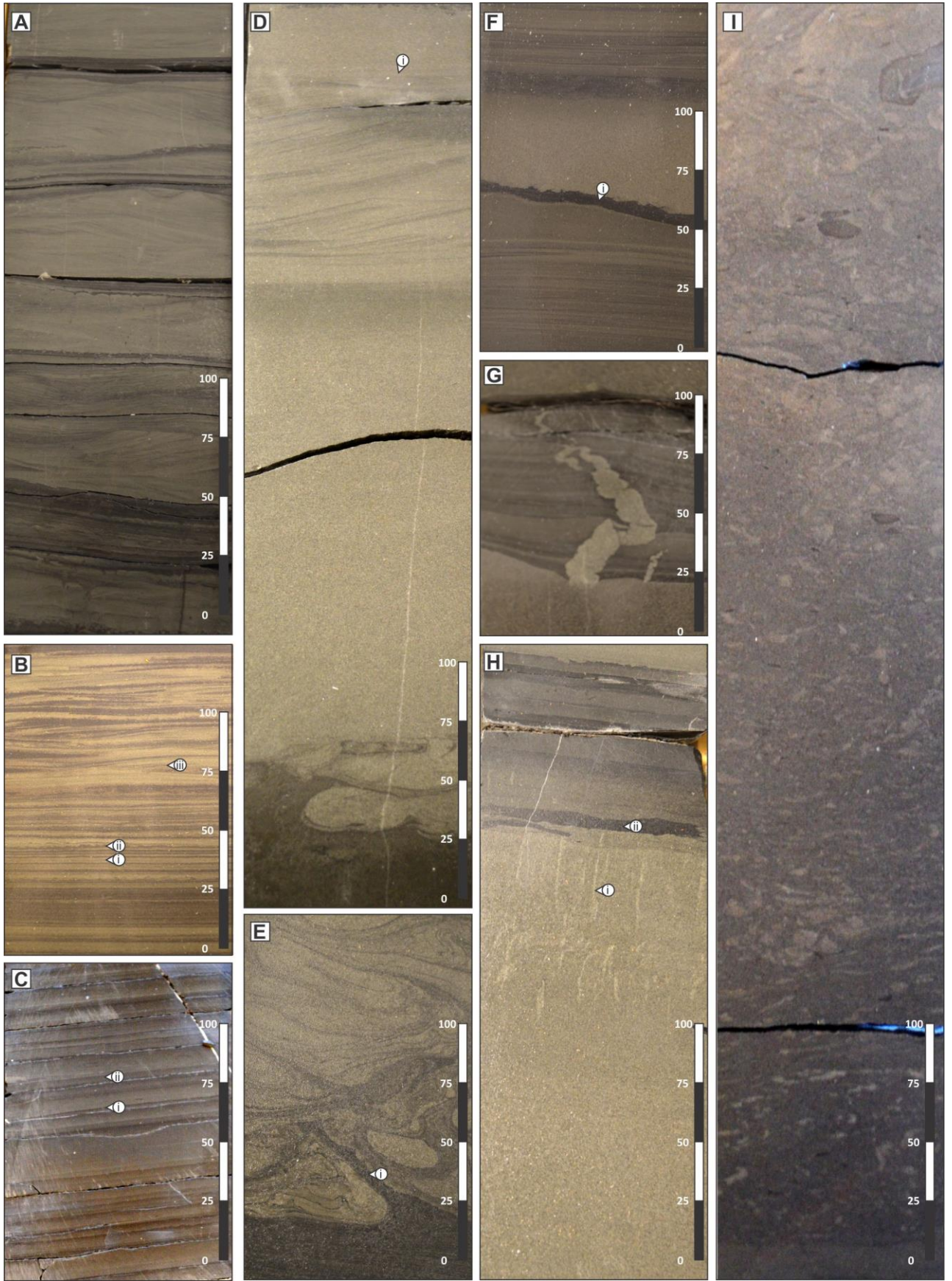
1180

1181

1182

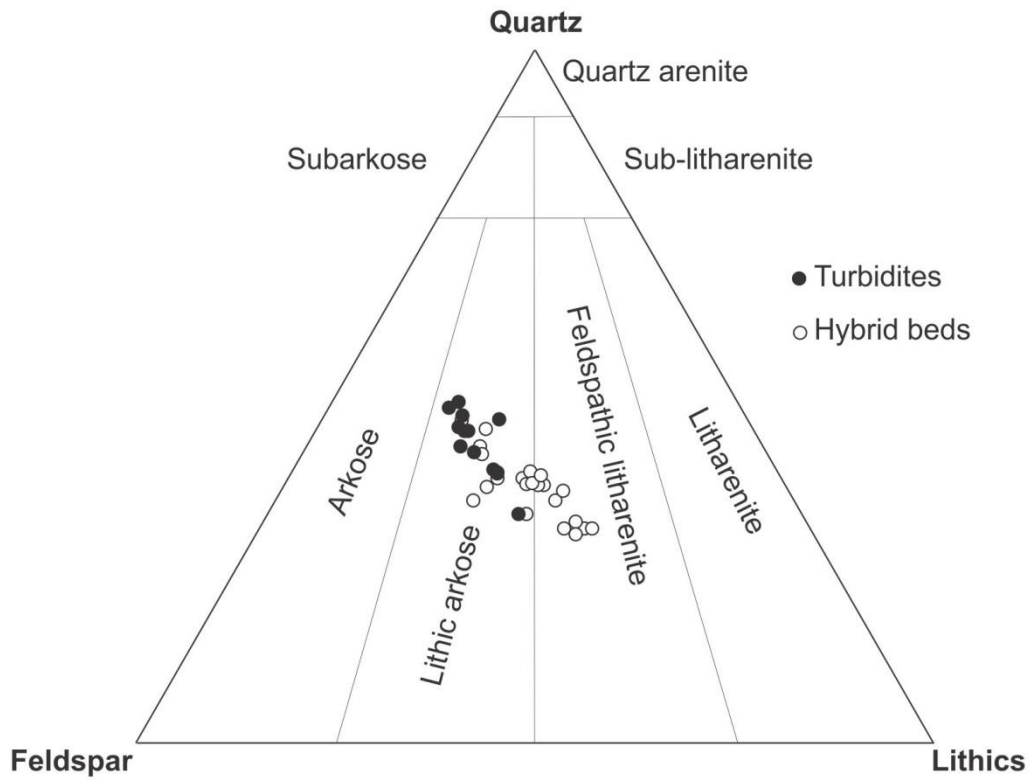
1183

Fig. 7. Representative hybrid bed photographs ('B' and 'T' symbols indicate base and top of beds). A) Bed showing intense interaction with the substrate and muddy upper part, these are typical in medial lobe settings. B & C) Hybrid beds with thick laminar/ high concentration flow deposits in their upper parts; these are typical in medial to distal settings. D) Hybrid beds with large rafts of siltstone and mudstone. E & F) Thin hybrid beds characteristic of the distal facies, with thin relatively clean sands at bed bases and overlying layers of varying mud content.

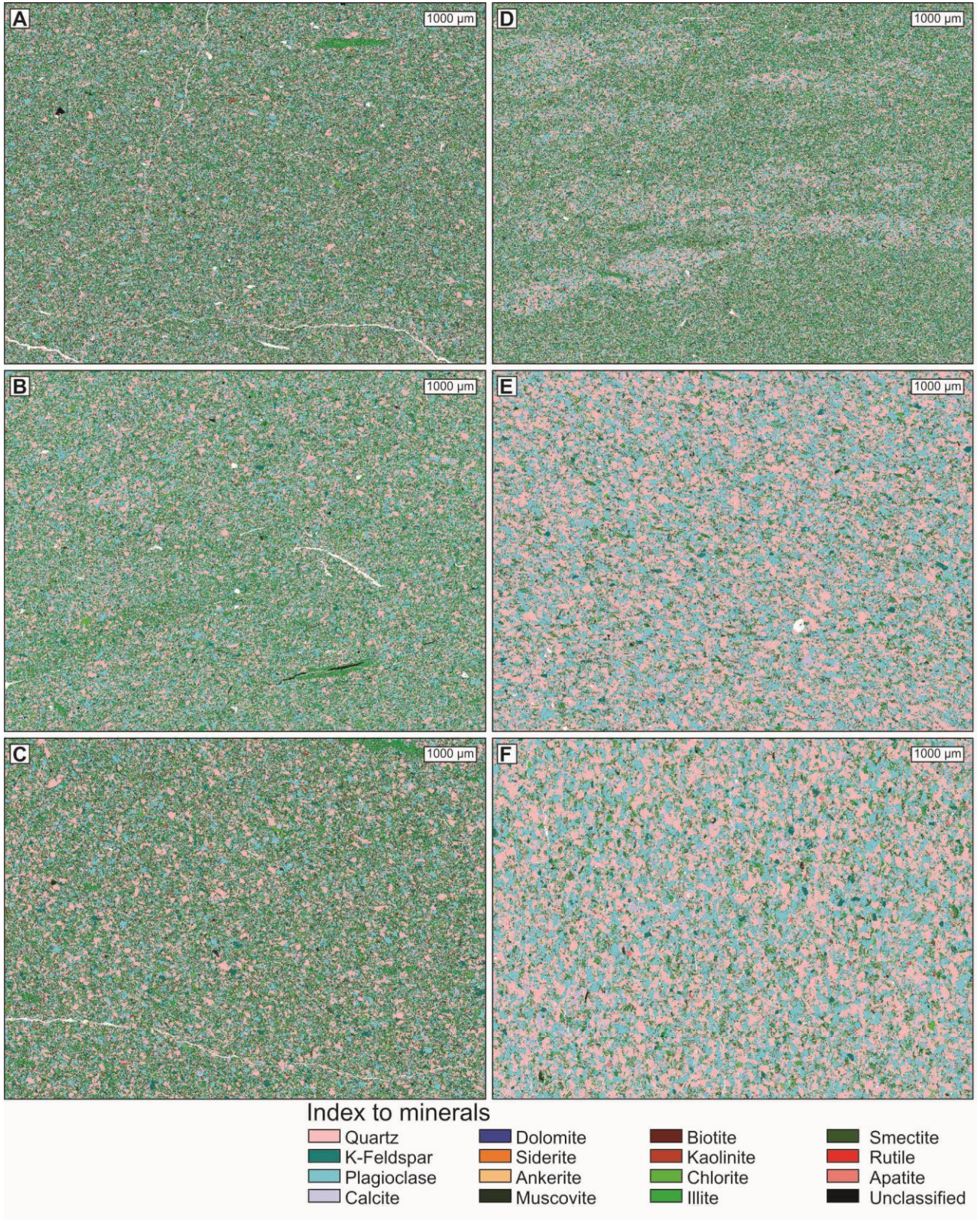


1184
 1185 Figure 8. Photographs from cores of representative facies. A) Thin-bedded low-density turbidites; B) Thinly-interbedded low-density turbidites
 1186 dominated by planar-lamination (i), small-scale load and flame structures (ii), and ripple-cross lamination (iii). C) Silty low-density turbidites graded
 1187 from medium silt (i) to very-fine silt (ii). D) Turbidite with loading and injection of the substrate at the base. The upper part of the bed is truncated (i).

1188 E) Detail of loading and deformation at the base of a turbidite. F) Muddy sandstone truncated by an erosion surface overlain by claystone (bypass
 1189 surface) and overlain by an argillaceous sandstone. G) Small injectite extending from a bed top. H) Dewatering pillars in the upper part of a hybrid bed,
 1190 (ii) large mudstone clasts. I) Thick debris with cleaner sandstone 'balls' and injections in an overall muddy sand matrix.

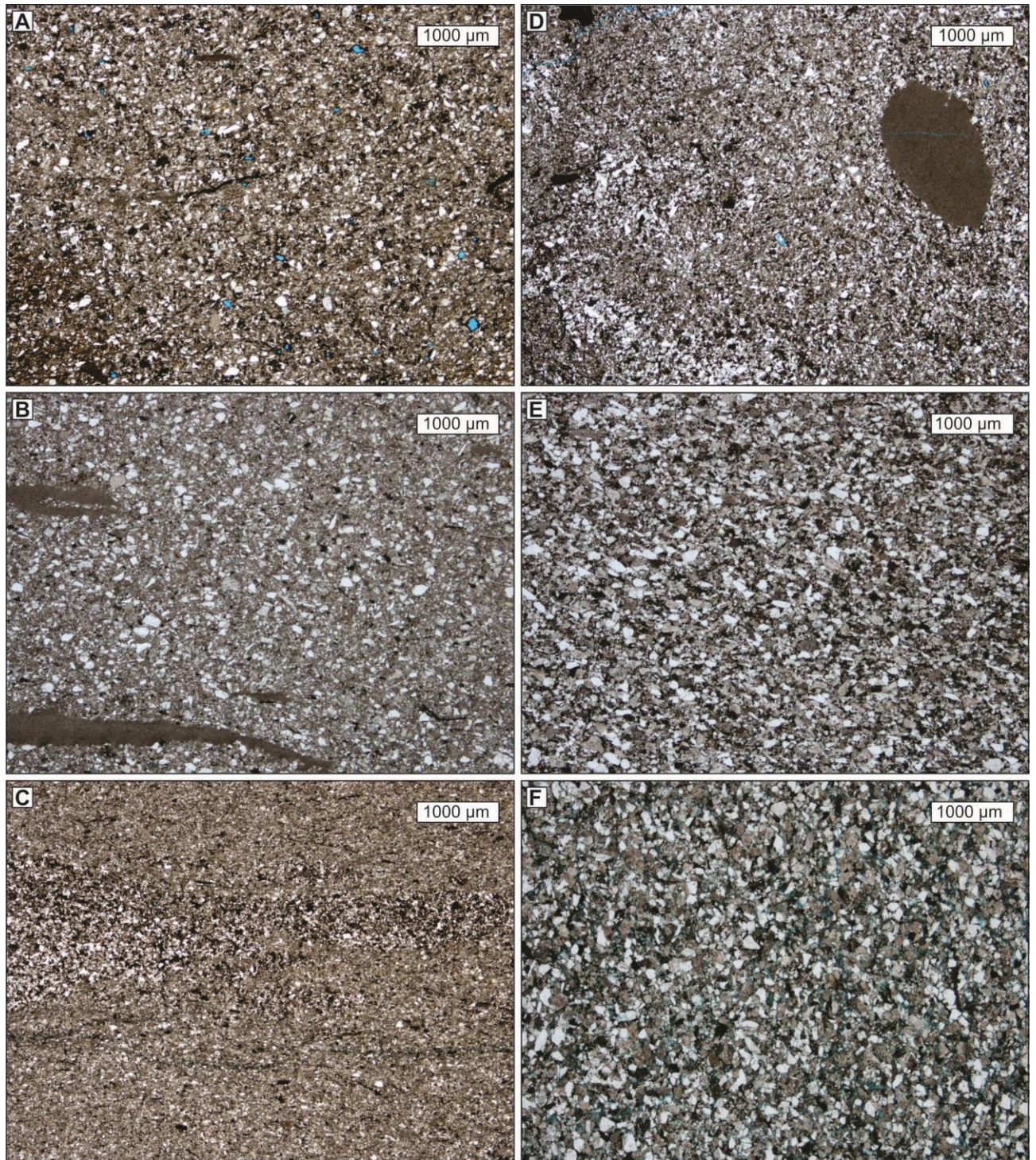


1191
 1192 Fig. 9. Quartz-feldspar-lithics (QFL) plot for samples subdivided into 'turbidites' and 'hybrid beds'. Turbidites fall entirely within the lithic arkose
 1193 class, whilst hybrid beds span the lithic arkose and feldspathic litharenite classes. Ternary plot from Folk (1974).



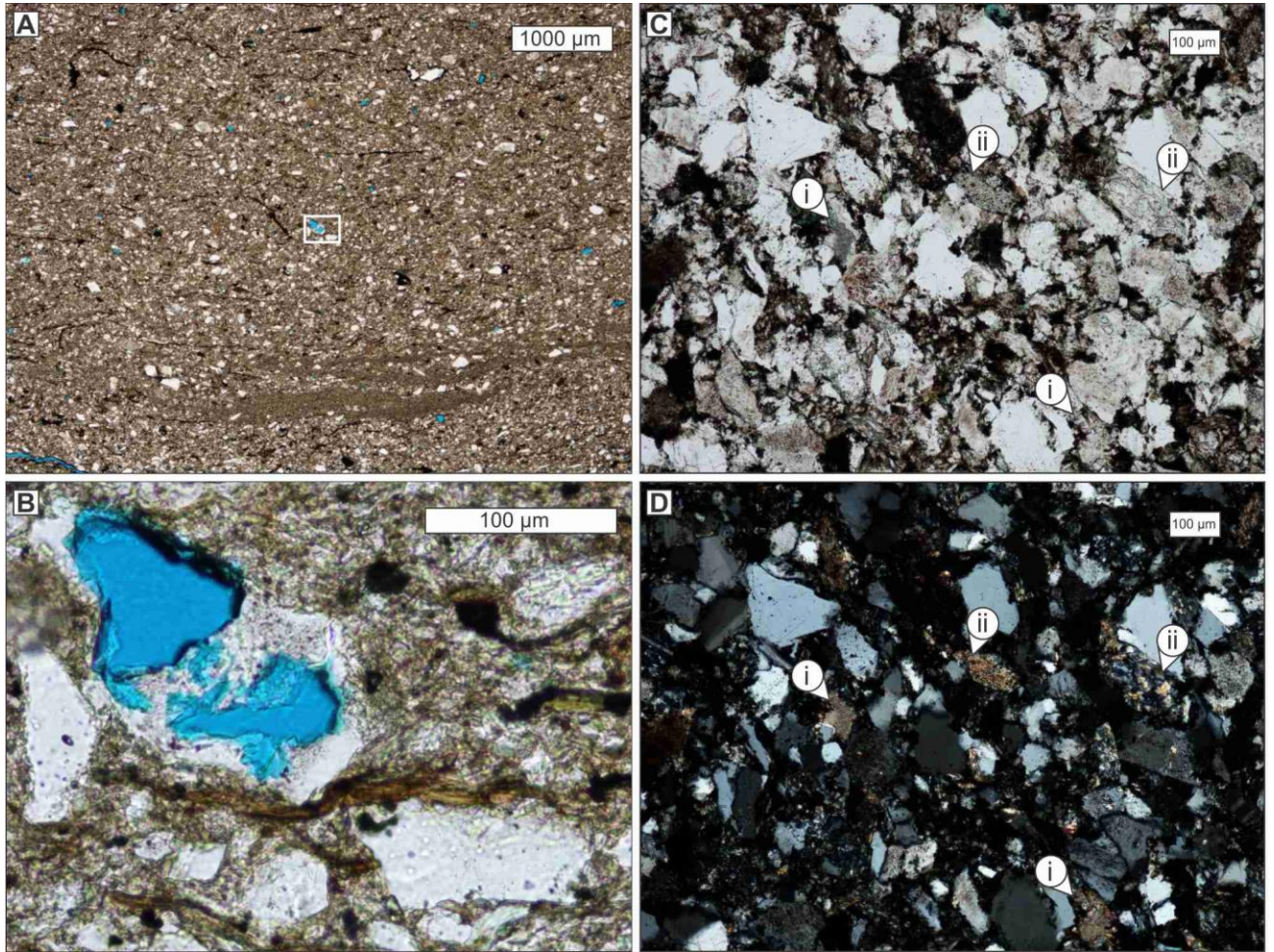
1194

1195 Figure 10. Mineral maps from thin-sections, based on chemical composition data from QEMSCAN. A-F show samples SK7A, B, C, D, H and I
 1196 respectively. SK7A-D are interpreted as hybrid beds whilst SK7H and SK7I are interpreted as turbidites (see table 1).



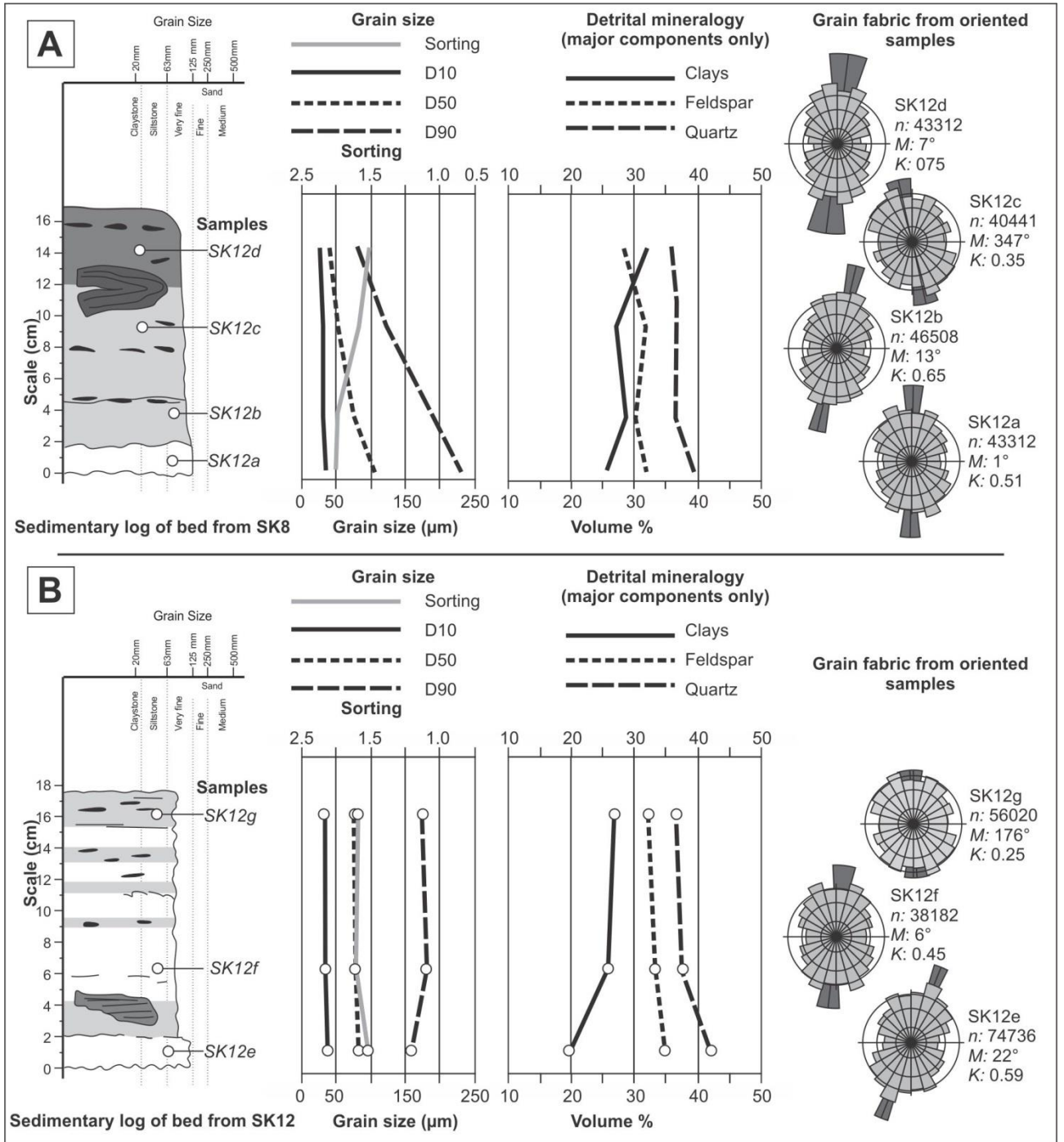
1197

1198 Figure 11. Representative thin-section photomicrographs. A) Sample SK7B: clay-rich sample from the middle part of a hybrid bed. Note the organic
 1199 fragments and porosity (blue) due to dissolution of framework minerals (probably feldspar). B) Sample SK7C: from the middle division of a hybrid
 1200 bed, this clay-rich sandstone has a strong bed-parallel grain fabric, with aligned claystone and organic clasts. C) Sample SK7D: Sample from a thick
 1201 muddy division within a hybrid bed, note the strong grain fabric with lens of coarser-grained sediment in the centre of the image. The sample lacks
 1202 visible porosity. D) Sample SK7E: Mixed 'swirled' fabric of relatively finer- and coarser-grained lenses. This sample is from a lighter coloured band in
 1203 a hybrid bed. The large rounded clast is a claystone. Note the porosity due to grain dissolution. E) Sample SK7H: This sample is from a tractional
 1204 sandstone with weak plane-parallel lamination, which has a much lower mud content than the previous examples, and an alignment of quartz and
 1205 feldspar grains along laminae. F) Sample SH7I. This sample is from the very-thick bed which caps Fan 3 at the SK7 locality. It does not appear to have
 1206 a strong grain fabric in thin-section and in outcrop lacks obvious tractional structure. The visible porosity is most-likely related to weathering processes
 1207 and fracturing around coarser grains.

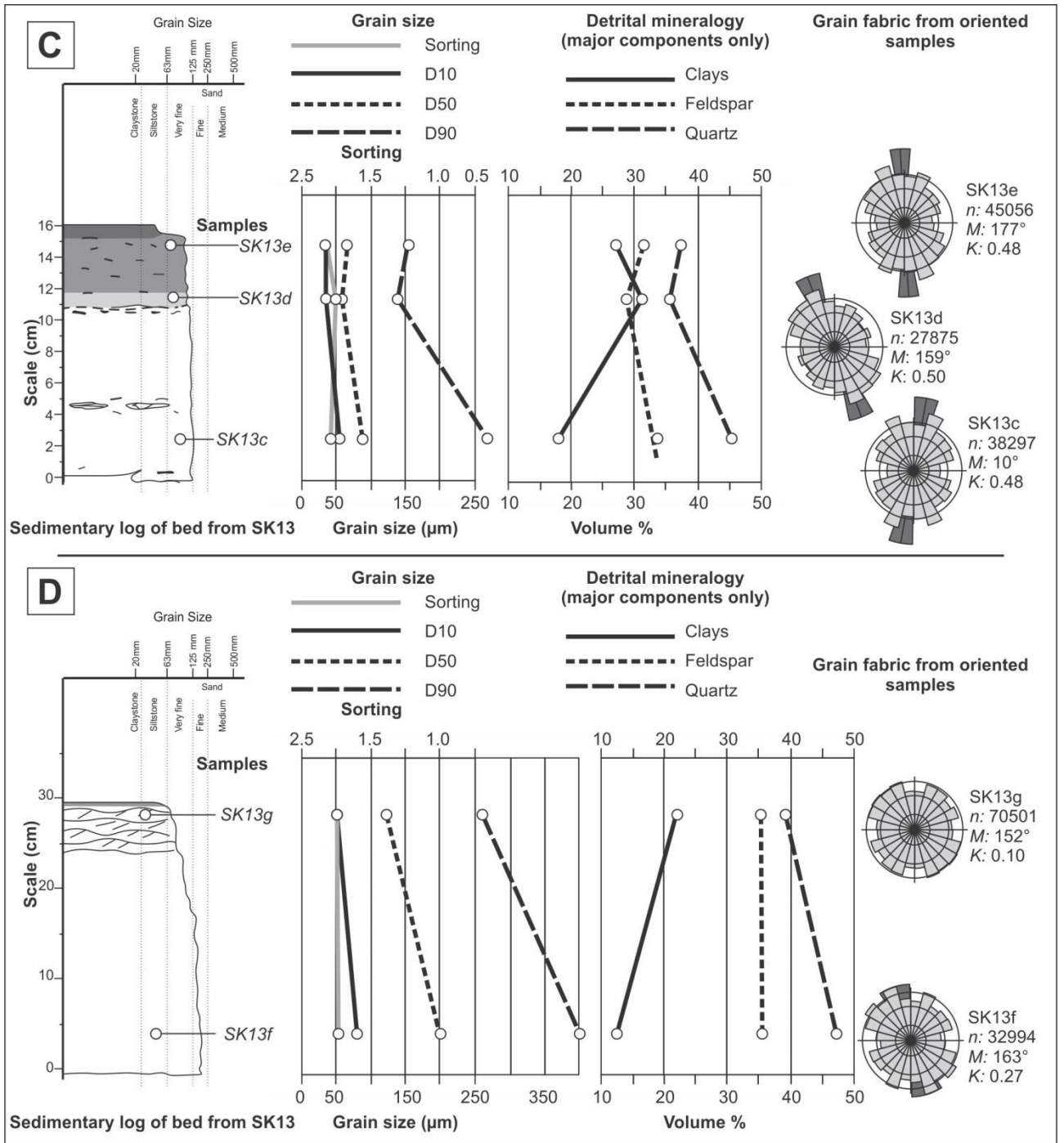


1208

1209 Figure 12. Thin-section photomicrographs in plane polarized light, from an argillaceous sandstone division of a hybrid bed (Sample SK7A, Log SK7.
 1210 A) Illustration of the very low degree of porosity in these rocks (blue colors indicate open pore spaces). B) The porosity that is present is
 1211 predominantly secondary, mostly through grain dissolution of feldspars; this example shows remnant grain material preserved. C&D) Sample SK7F,
 1212 interpreted as a hybrid bed. Thin section micrographs in plane polarized light (C) and with crossed polars (D). These images clearly show the abundant
 1213 rock fragments which are common in all of the sampled rocks. Some fragments appear to be of carbonate rocks (I), although discrimination from
 1214 altered plagioclase can be difficult, whilst others are composed of multiple minerals (II); calcite is recorded in the QEMSCAN mineralogical analysis
 1215 for this sample.



1216



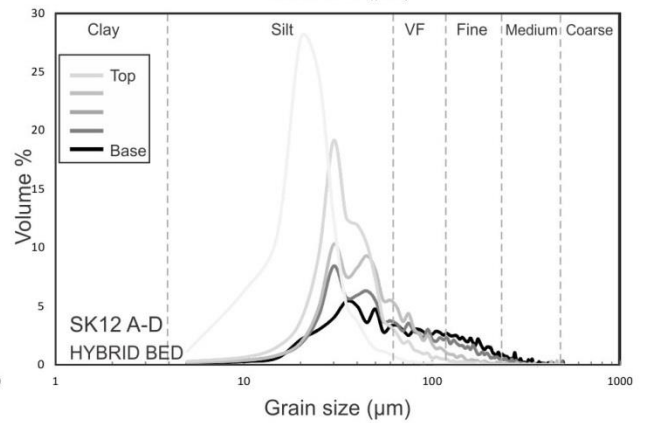
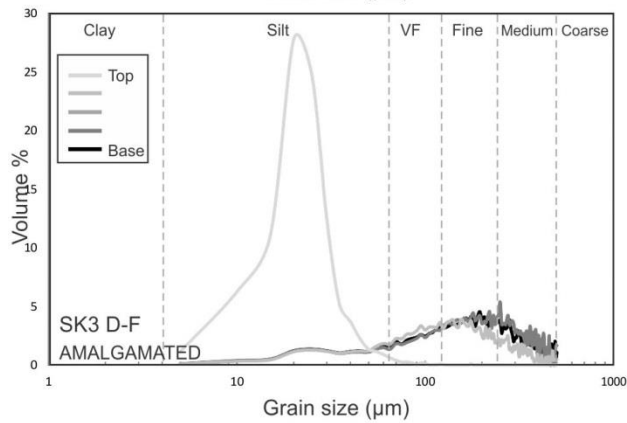
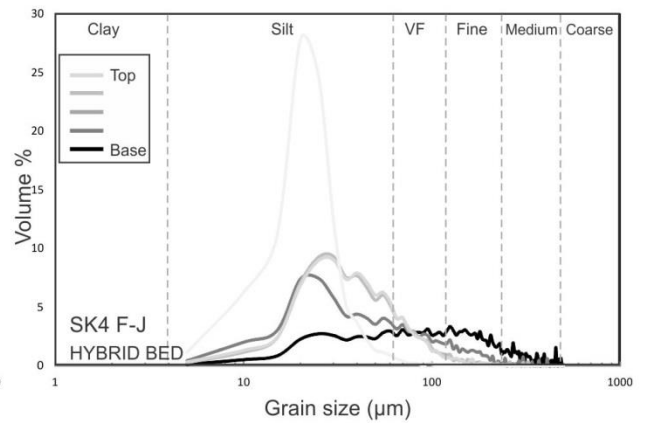
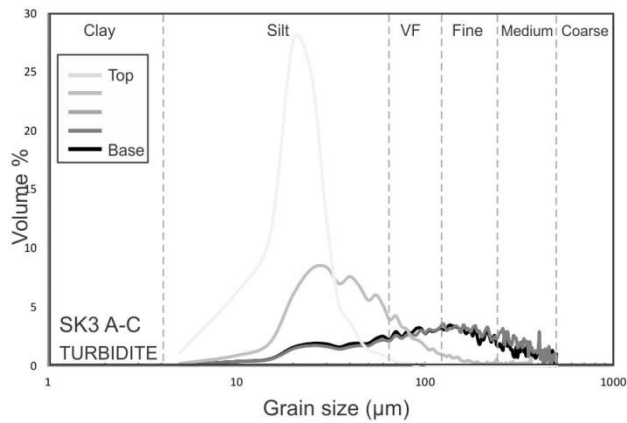
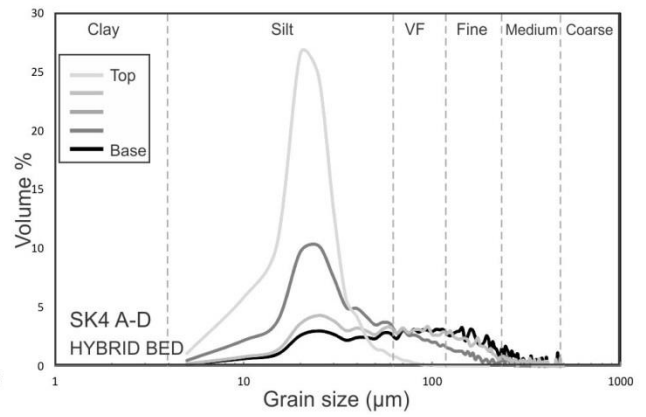
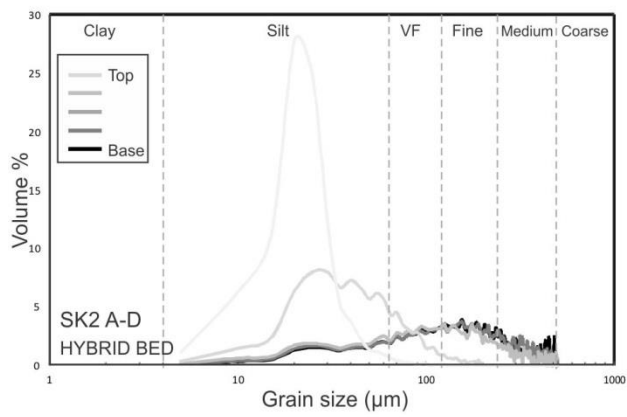
1217

1218

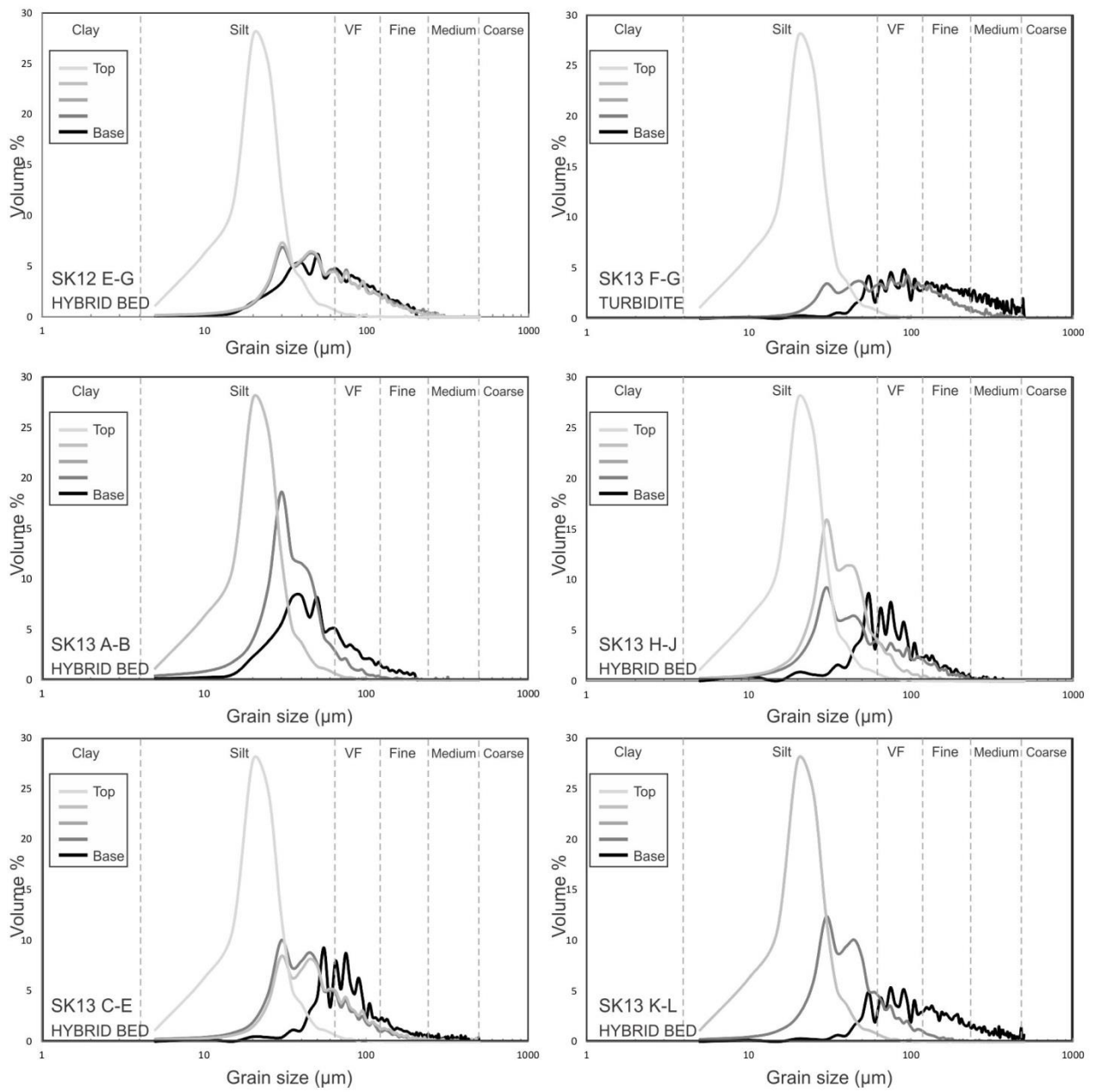
1219

1220

Figure 13. Summary diagrams illustrating grain-size trends, sorting, mineralogy and grain fabric for representative examples of hybrid beds (A, B, C) and one turbidite (D). Note that the straight lines between data points are for illustration only and do not indicate that data points can necessarily be extrapolated.



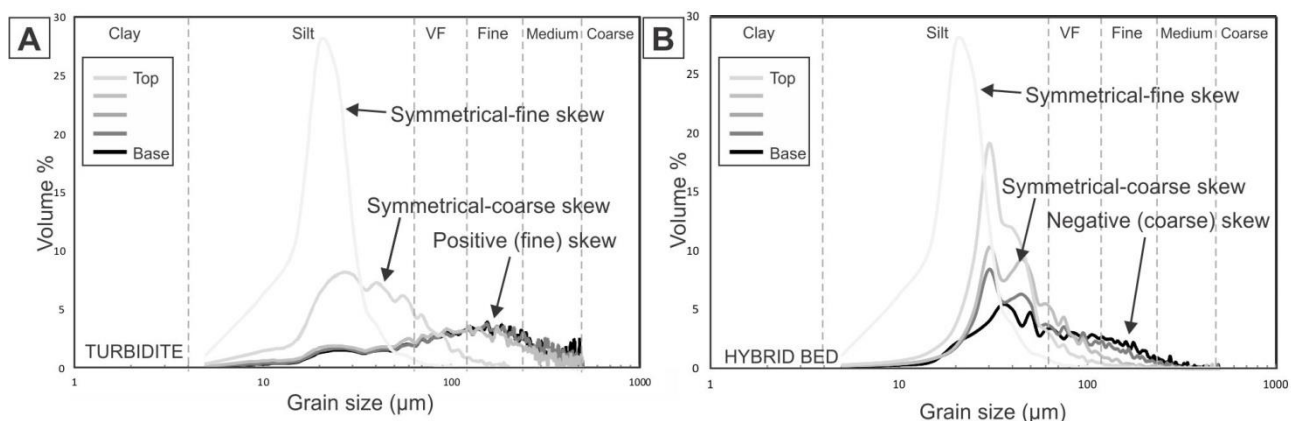
1221



1222

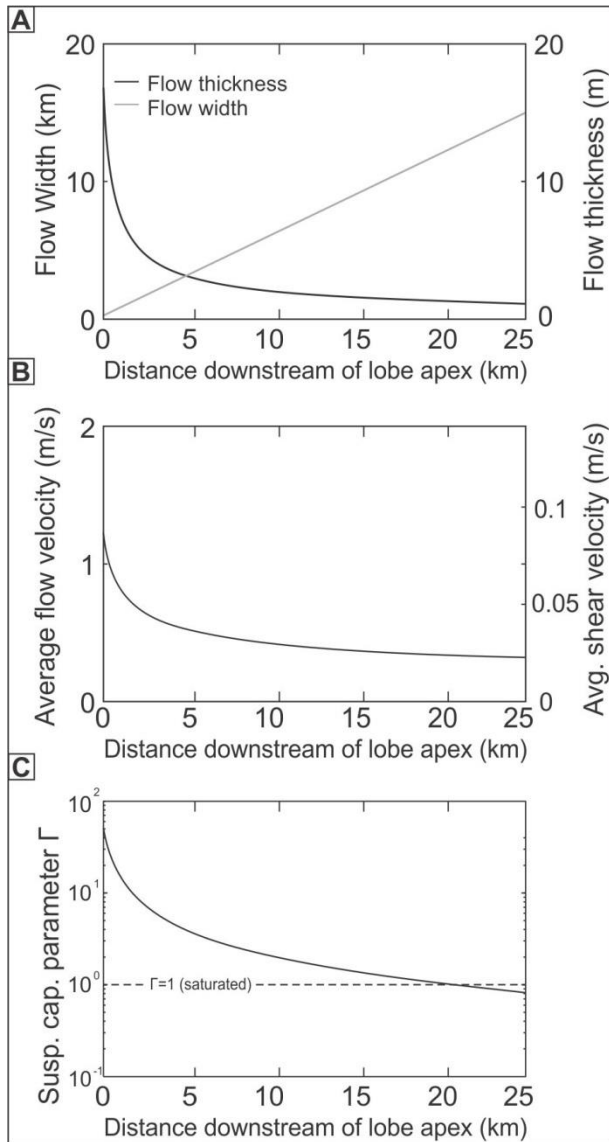
1223
1224
1225

Figure 14. Grain-size distribution curves for individual hybrid and turbidite beds. Whilst the grain size curves are largely distinctive for the different flow types (summarised in Fig. 15), SK2 although described as a hybrid bed has much the same character as a turbidite, albeit slightly enriched in coarser grains and with a more clay rich top (see Table 1).



1226
 1227 Figure 15. Representative grains-size distribution for deposits described as A) turbidites and B) hybrid beds. Turbidites are characterised by positively
 1228 (fine) skewed lower bed divisions, and typically symmetrical upper divisions; in contrast, hybrid beds are characterised by negative (coarse)
 1229 lower divisions and symmetrical to coarse upper divisions.

1230
 1231
 1232
 1233



1234

1235

1236

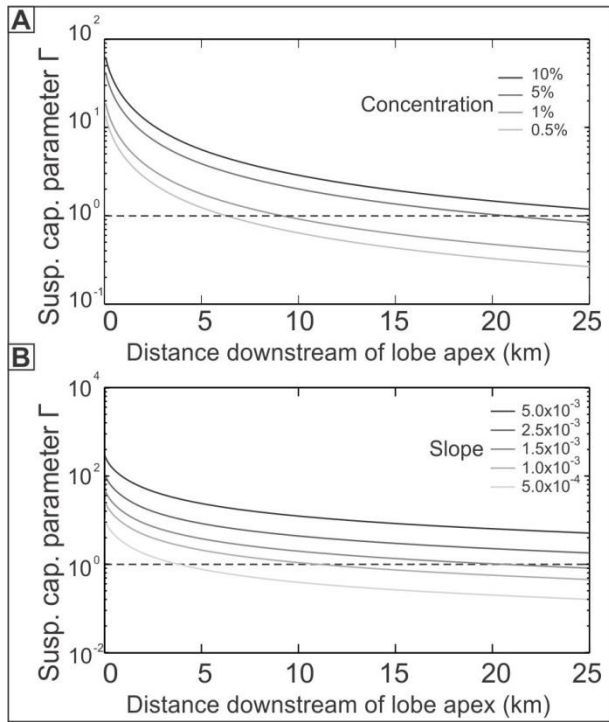
1237

1238

1239

1240

Figure 16. Flow parameters along lobe length for a scenario where channel width is 250 m; channel depth and initial flow thickness are 13 m and 17 m respectively; flow concentration is 5%; slope is $1.5 \cdot 10^{-3}$; lobe width is 15 km; lobe length is 25 km. (A) Flow width increases linearly over the lobe length from the channel width at the lobe apex to the full lobe width. Flow thickness decreases rapidly proximally, and more slowly distally. (B) Average velocity (left y-axis) and bed-shear velocity (right y-axis). Plots overlap because the drag coefficient has been used to normalise the right y-axis according to Eq. (4). (C) Suspension capacity parameter Γ is much larger than 1 at the lobe apex, indicating undersaturated near-bed conditions, reaches the threshold value of $\Gamma=1$ 21 km downstream of the lobe apex, and $\Gamma < 1$, leading to turbulence suppression, downstream of 21 km.



1241

1242

1243

1244

Figure 17. The sensitivity of the downstream evolution of Γ to different estimations for inlet concentration and slope. (A) Sediment concentrations of 10%, 5%, 1%, and 0.5%; for a given slope, the distance to flow transformation increases with increasing sediment concentration. (B) Slope gradients of 5.0×10^{-3} , 2.5×10^{-3} , 1.5×10^{-3} , 1×10^{-3} , and 5.0×10^{-4} ; for a given concentration, the distance to flow transformation increases with increasing slope.

1245

1246

1247

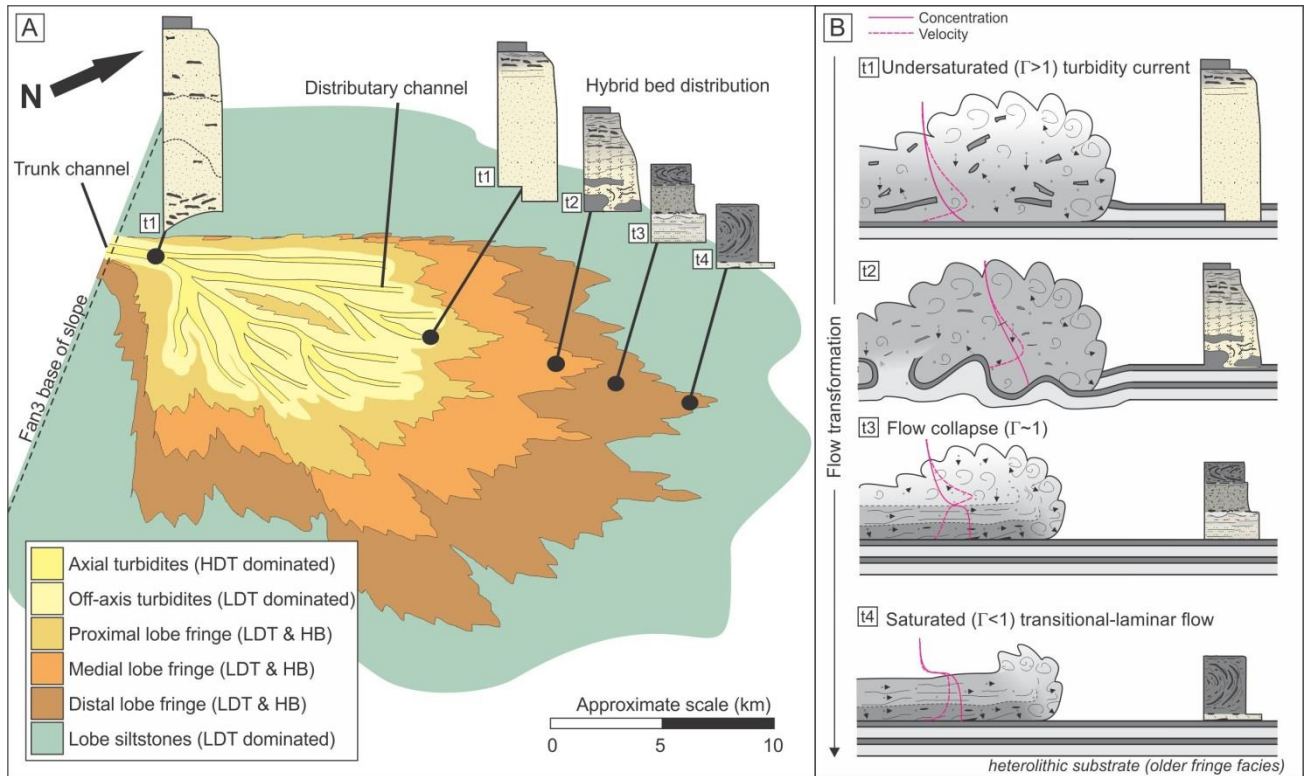
1248

1249

1250

1251

1252



1253

1254 Figure 18. A) Schematic perspective/plan view of Fans 3. The distribution of hybrid beds is illustrated with schematic logs (see 'B'), but note that the
 1255 fan fringe is not limited to hybrid beds, low-density turbidites are also common. At t₀, in the trunk channels, flows are undersaturated with respect to
 1256 the flow suspension capacity ($\Gamma > 1$) and strongly erosional; high density turbidites are amalgamated and can be mudstone-clast rich. B) Summary
 1257 diagram of flow evolution and deposit type for flows in the fringe area which start out, at t₁, fully turbulent and well mixed and undersaturated ($\Gamma > 1$),
 1258 capable of eroding and entraining substrate. As flows decelerate from the channel-lobe transition (t₂), shear stress exerted on the bed decreases, leaving
 1259 substrate interaction preserved and resultant deposits clast and mud rich. Further deceleration and enrichment in cohesive and fine grained material (t₃)
 1260 results in the concentration profile becoming increasingly stratified and, when flows drop below the critical value of $\Gamma = 1$ they are oversaturated and
 1261 suspension capacity is lost. A dense lower layer forms, which continues to move downstream owing to its high water content (due to clays and very
 1262 fine silts), grains are supported by yield strength but coarser grains settle resulting in a relatively well sorted sand fraction within a mud-rich matrix.
 1263 Overlying layers are muddier and less well sorted. The formation of this high concentration lower boundary layer flow inhibits the transmission of
 1264 turbulent kinetic energy into the upper part of the flow and turbulence is rapidly dissipated (t₄).

1265

1266